https://doi.org/10.5194/egusphere-2026-5709
Preprint. Discussion started: 3 November 2026
© Author(s) 2026. CC BY 4.0 License.

Selective Impacts of Prior, Background-Concentration, and Observation-Error Assumptions on Urban CO_2 Inversion Estimates

Munsu Park[1], Sujong Jeong[1], Sojung Sim[2]

[1]Department of Environmental Management, Graduate School of Environmental Studies, Seoul National University, Seoul, 08826, Republic of Korea
[2]Environmental Planning Institute, Seoul National University, Seoul, 08826, Republic of Korea

Correspondence to: Sujong Jeong (sujong@snu.ac.kr)

Abstract. Urban-scale CO_2 inversions are increasingly used to constrain fossil fuel CO_2 emissions; however, posterior estimates can depend on the methodological assumptions used to define key inversion parameters. How these assumptions selectively affect different aspects of posterior information remains unclear. Here we quantify the impacts of prior emissions, background concentrations, and observation-error covariance assumptions on urban CO_2 inversion results. Using wintertime Seoul, South Korea, as a case study to minimize biogenic flux uncertainties, we conducted 18 Bayesian inversions by combining two prior emission inventories, three background concentration definitions, and three observation-error estimation methods. We found that these assumptions affect distinct components of posterior emissions: the spatial distribution of posterior estimates was primarily controlled by the choice of prior, whereas total emissions and their temporal variability were more strongly influenced by observation-error and background-concentration assumptions. The spread in posterior estimates arising from these methodological assumptions ranged from 25.6 % to 51.5 % of total emissions, exceeding the posterior uncertainty estimated within individual inversion configurations. This result indicates that uncertainty estimates from a single inversion setup may not fully capture the methodological uncertainty associated with input assumptions. Using parameter sensitivity and an uncertainty reduction metric, we further identified a relatively robust configuration for the Seoul winter daytime case and evaluated whether the inversion reduced the spread among the estimates relative to the prior spread. Our results demonstrate that methodological assumptions can selectively shape urban CO_2 inversion estimates and highlight the need to assess their impacts when interpreting posterior emissions.

1 Introduction

Urban areas cover approximately 3 % of the Earth but are home to 45 % of the world's population (Liu et al., 2014; Ritchie et al., 2024). Approximately 75 % of global energy consumption and 70 % of energy-related CO_2 emissions are generated in urban areas (IEA, 2024; Seto et al., 2014). By 2050, cities are projected to accommodate two-thirds of global growth, thereby exerting an increasingly significant impact on national CO_2 emissions (Luqman et al., 2023; United Nations, 2025). Consequently, the management of urban CO_2 emissions has emerged as a critical strategy for effective global carbon reduction. Along with this need, the critical role of city-level actions in reducing greenhouse gas emissions was emphasized at COP21 in

https://doi.org/10.5194/egusphere-2026-5709
Preprint. Discussion started: 3 November 2026
© Author(s) 2026. CC BY 4.0 License.

Paris (UNFCCC, 2016). The European Union launched the "Climate-Neutral and Smart Cities", selecting 112 European cities as innovation hubs to advance carbon neutrality across the continent (European Commission, 2025). Similarly, the Cities Climate Leadership Group (C40), a network of 96 cities worldwide, provides the Climate Action Planning Program and supports joint efforts to achieve a 50 % reduction in emissions by 2030 (C40, 2025). To effectively support such urban CO_2 management strategies, it is essential to develop a robust understanding of urban CO_2 emissions. Accurate emission data that capture spatiotemporal characteristics enable the identification of major sources, prioritization of reduction strategies, and evaluation of policy effectiveness.

To understand urban carbon emissions, the bottom-up approach ("inventories") has been widely used to estimate emissions (Arioli et al., 2020; Gilfillan and Marland, 2021). This approach quantifies emissions by collecting activity data such as fuel consumption, traffic volume, and energy use, and then applies emission factors through statistical methods. The resulting inventories enable sector-specific emission analyses that help characterize urban emission patterns and inform appropriate mitigation strategies. For instance, the bottom-up approach has identified dominant emission sectors, such as power plants, heating, and building energy use (Cai et al., 2020; Sówka and Bezyk, 2018). Inventories have also been analyzed together with demographic or air-pollution data to examine the drivers and associated characteristics associated with increasing CO_2 emissions, such as population, urban sprawl, and air-pollutant sources, and to support city-specific mitigation strategies (Luqman et al., 2023; Shahbazi et al., 2022).

Bottom-up approaches offer the advantage of providing urban carbon emissions at high resolution, reflecting local characteristics. However, considerable time is required to compile emission estimates, resulting in time lags. These time gaps can create delays in policy adoption, rendering appropriate reduction responses challenging. Uncertainties in bottom-up inventories have also been addressed. Obtaining reliable activity data at finer resolution is challenging and lead to substantial data gaps (Gurney et al., 2019; Newman et al., 2016). This challenge is particularly severe in developing countries, where the availability of reliable, high-quality data remains limited (Bai et al., 2018). Furthermore, inventories derived by downscaling global emissions data using spatial proxies are prone to misallocation of point sources and uncertainties inherent in the proxy data themselves. Consequently, bottom-up approaches exhibit uncertainties ranging from 50 to 250 % in urban emission estimates (Gately and Hutyra, 2017). Such inaccuracies can obscure the identification of major urban emission sources and thereby hinder the design, implementation, and evaluation of effective mitigation strategies.

Recently, inverse modeling has emerged as a promising top-down approach for independently verifying and improving emission inventories. By constraining inventories with atmospheric observations and atmospheric transport models, this approach has been applied in many cities to evaluate inventories and reduce their uncertainties, including Tokyo (Ohyama et al., 2023), Beijing (Che et al., 2022), Seoul (Sim and Jeong, 2025), Salt Lake City (Kunik et al., 2019; Mallia et al., 2020), Mexico City (Che et al., 2024), Washington D.C (Lopez-Coto et al., 2020), Indianapolis (Lauvuax et al., 2016), New York City (Pitt et al., 2022), and Paris (Nalini et al., 2022). Additionally, inverse modeling has been conducted to detect emission changes from events such as COVID-19 in Paris (Nalini et al., 2022) and sporadic sources such as wildfires in the California Bay Area (Hamilton et al., 2024). More recently, inverse modeling has been extended to characterize urban emission patterns

https://doi.org/10.5194/egusphere-2026-5709
Preprint. Discussion started: 3 November 2026
© Author(s) 2026. CC BY 4.0 License.

through sector-specific emission adjustments, such as those in Indianapolis (Nathan et al., 2018), Paris (Nalini et al., 2022), and the Los Angeles Basin (Roten et al., 2023).

The use of inverse modeling has increased; however, this approach requires numerous input variables and assumptions, that can influence the resulting emission estimates (Chandra et al., 2022; Lauvaux et al., 2016; Zhang et al., 2024). Although such sensitivity has also been reported at the regional and national scales, it is likely to be even more pronounced at the urban scale, where emissions are resolved at finer resolution and estimates depend more sensitively on modelling assumptions (Zhang et al., 2024). For example, sensitivity analyses conducted within individual studies have shown that differences in model configuration values can lead to substantial discrepancies in urban emission estimates. In the Indianapolis flux experiment, differences in model parameter values introduced systematic uncertainties of up to 25 % even for the same city (Lauvaux et al., 2016). Similarly, studies estimating the 2019 CO_2 emissions in Paris showed different values of 3.53, 5.75, and 9.21 Mt CO_2 depending on the methods for background concentration definitions and the spatial correlation length of prior errors (Lian et al., 2023; Nalini et al., 2022).

This sensitivity is likely to be further amplified by differences in the estimation of key input variables across urban inverse modelling studies. At the urban scale, approaches used to estimate key inputs vary considerably among studies. For prior emissions, recent studies have utilized CO_2 emissions inventories ranging from global datasets (e.g., Open-source Data Inventory for Anthropogenic CO_2 (ODIAC) and the Emission Database for Global Atmospheric Research (EDGAR)) to region-specific datasets (e.g., Origins.Earth for Ile-de-France, Hestia for Salt Lake City, and Vulcan for U.S cities), with certain studies incorporating multiple inventories across spatial scales. Background concentration definitions also differ substantially, between percentile-based statistical approaches and methods that use high-altitude site measurements. Similarly, observation error assumptions vary across studies, including approaches based on residual error, diagnostics, and the summation of error methods.

Despite these differences, relatively few studies have focused on how variations in input estimation approaches affect inversion results at the urban scale. At global and regional scales, coordinated inverse model intercomparison studies, such as TransCom 3, RECCAP, and OCO-2 MIP, have been conducted to systematically identify and reduce discrepancies across different modelling frameworks (Crowell et al., 2019; Gurney et al., 2003; Kong et al., 2022; Peylin et al., 2013). However, comparable efforts at the urban scale remain limited. Most previous studies have focused on estimating constrained emissions using a single set of methodological assumptions, evaluating sensitivity only by adjusting parameter values within that framework. However, this approach cannot fully capture the differences in emission estimates arising from fundamentally different input assumptions across studies. Indeed, this limitation has been discussed in previous studies, which emphasized the need for explicit comparisons across different methodological configurations (Cai et al., 2025).

Thus, this study aims to provide a quantitative assessment of how different methodological assumptions for input parameters affect urban CO_2 emissions estimates. We focus on a methodological sensitivity experiment by comparing emission estimates derived under different assumption configurations. This enables us to examine how methodological choices for each parameter

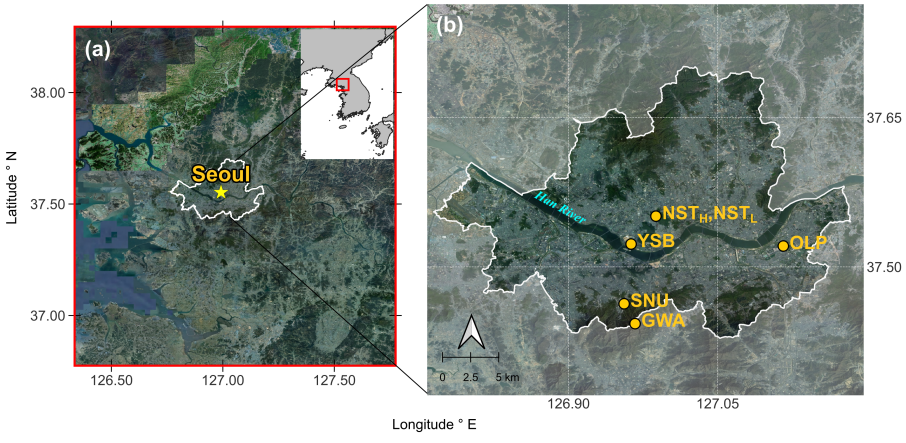
https://doi.org/10.5194/egusphere-2026-5709
Preprint. Discussion started: 3 November 2026
© Author(s) 2026. CC BY 4.0 License.

influence the different aspects (e.g., total fluxes and spatiotemporal variability) of posterior emissions and identify the uncertainty arising from these assumption choices.

Seoul is a densely populated megacity characterized by substantial CO_2 emissions, complex topography, and diverse land-use patterns. The Han River bisects the city and forests cover 25.3 % of its total area (Korea Forest Service, 2021), reflecting its heterogeneous urban environment. This natural complexity combined with diverse land-use types, results in large spatiotemporal heterogeneity of emission sources, with annual CO_2 fluxes ranging from 1.09 kg C m^{-2} yr^{-1} to 16.28 kg C m^{-2} yr^{-1} across different urban land-use categories (Park et al., 2022; Hong et al., 2023). Given this complexity, methodological assumptions in inverse modelling are expected to have a distinct influence on emissions estimates. Consequently, such variability makes Seoul a suitable testbed for systematically evaluating the sensitivity of urban-scale inversion results to different parameter assumptions. Using Seoul as a case study, the primary objective of this study is to systematically identify how the choice of input estimation approaches affects CO_2 emission estimates within an urban inverse modelling framework.

2 Materials and Methods

This section describes the inverse methodology, input data used in the inversions (including both common and varying components), experimental design, and analytical methods used in this study. Building on the Bayesian inverse modelling framework for Seoul (Sim and Jeong, 2025), this study revisited the December 2021 case by focusing on methodological comparisons among the estimation approaches for prior emissions, background concentrations, and observation error covariances. December provides a controlled wintertime period in which uncertainties in biogenic fluxes are expected to be minimized. The inversion was conducted at a fine scale with a spatial resolution of 0.01°×0.01° and a temporal resolution of 1 h. The Seoul domain and outer domain used in the inversion system are illustrated in Fig. 1.



https://doi.org/10.5194/egusphere-2026-5709
Preprint. Discussion started: 3 November 2026
© Author(s) 2026. CC BY 4.0 License.

Figure 1. Map of Seoul, including six ground-based observation sites: Gwanak Mountain (GWA), N Seoul Tower-High (NST_H), N Seoul Tower-Low (NST_L), Yongsan Building (YSB), Olympic Park (OLP), and Seoul National University (SNU). (a) Outer domain for biogenic fluxes in Seoul, outlined by the red box. (b) Distribution of the six observation sites (yellow circles) within the unshaded region, representing the study domain, Seoul. The base map was obtained from VWorld Satellite Imagery, Ministry of Land, Infrastructure and Transport, Republic of Korea.

2.1 Inverse Methodology

In this study, our Bayesian inverse framework assimilates atmospheric CO_2 observations to optimize prior CO_2 emissions by accounting for uncertainties in both observations and prior emissions. By minimizing the mismatch between the observed and modeled CO_2 enhancements from prior and the deviation from the prior emissions, the cost function is expressed as follows in Eq. (1) (Enting, 2002; Tarantola, 1987):

$$L_s = \frac{1}{2}(\boldsymbol{z} - \mathbf{H}\boldsymbol{s})^T \mathbf{R}^{-1}(\boldsymbol{z} - \mathbf{H}\boldsymbol{s}) + \frac{1}{2}\left(\boldsymbol{s} - \boldsymbol{s}_p\right)^T \mathbf{Q}^{-1}(\boldsymbol{s} - \boldsymbol{s}_p) \quad (1)$$

The solution that minimizes this cost function L_s , called the posterior CO_2 emission estimates ($\hat{s}$), is described as Eq. (2) (Rodgers, 2000):

$$\hat{\boldsymbol{s}} = \boldsymbol{s}_p + (\mathbf{HQ})^T(\mathbf{HQH}^T + \mathbf{R})^{-1}(\boldsymbol{z} - \mathbf{H}\boldsymbol{s}_p) \quad (2)$$

Where $\boldsymbol{s_p}$ is the prior vector of anthropogenic CO_2 fluxes with dimensions ($m \times 1$), with m equal to the number of grid cells in the study domain multiplied by the number of flux-data timesteps in this study. **H** is the Jacobian matrix of the footprint values obtained from the atmospheric transport model, with dimensions ($n \times m$), where n is the number of assimilated observations. This matrix serves as the observation operator, quantifying the sensitivity of the observed enhancements at the measurement sites to surface emissions. **Q** ($m \times m$) is the prior error covariance matrix, and **R** ($n \times n$) is the observational error covariance matrix. The vector $\boldsymbol{z}$ is the observed anthropogenic CO_2 enhancements with dimensions ($n \times 1$), corresponding to the CO_2 concentrations attributable to anthropogenic CO_2 emission sources.

For calculating the enhancement $\boldsymbol{z}$, we defined $\boldsymbol{z}$ as Eq. (3):

$$\boldsymbol{z} = \boldsymbol{z}_{obs} - \boldsymbol{z}_{bg} - \mathbf{H}\boldsymbol{s}_{bio} \quad (3)$$

Where $\boldsymbol{z_{obs}}$ represents the dataset from the observation sites and $\boldsymbol{z_{bg}}$ is the background concentration. To separate biological influences, the biogenic CO_2 enhancement was calculated by multiplying the biogenic CO_2 fluxes $\boldsymbol{s_{bio}}$ by the matrix **H**.
The uncertainty of the posterior emission estimates can be described using Eq. (4):

$$\mathbf{V}_{\hat{\mathbf{s}}} = \mathbf{Q} - (\mathbf{HQ})^{\mathrm{T}}(\mathbf{HQH}^{\mathrm{T}} + \mathbf{R})^{-1}(\mathbf{HQ}) \quad (4)$$

https://doi.org/10.5194/egusphere-2026-5709
Preprint. Discussion started: 3 November 2026
© Author(s) 2026. CC BY 4.0 License.

2.2 Common Input Data

2.2.1 Ground-Based Observations

Six measurement sites within the Seoul CO_2 observational network were used in this study, as shown in Fig. 1b (yellow markers). Gwanak Mountain (GWA) and Seoul National University (SNU) are located in southern Seoul. The N Seoul Tower-High (NST_H), N Seoul Tower-Low (NST_L), and Yongsan Building (YSB) are situated in central Seoul, while Olympic Park (OLP) is located in eastern Seoul. GWA and NST_H are considered suitable for capturing CO_2 enhancements originating from outside Seoul. GWA is located in an outlying area with no nearby sources. Although the NST_H is located in central Seoul, its inlet is situated above the nocturnal Planetary Boundary Layer Height (PBLH), allowing it to predominantly reflect inflow from outside Seoul during nighttime. YSB is surrounded by commercial areas, whereas OLP is influenced by nearby traffic sources. SNU and NST_L are located near vegetated areas. GWA, NST_L, and OLP were equipped with cavity ring-down spectroscopy instruments, whereas NST_H, YSB, and SNU were equipped with SNUCO2M instruments employing non-dispersive infrared absorption (Li-850). The instrument information, location, above ground level (AGL) of inlet heights, and mean daytime CO_2 concentrations for the six sites are summarized in Table 1. Each site exhibits different distributions influenced by the surrounding CO_2 emission sources and the AGL of the inlet. The GWA and NST_H sites, with relatively high inlet heights, exhibited lower CO_2 concentrations and smaller variability. YSB, which is located in central Seoul and is sensitive to various emission sources, recorded high concentrations with large variability.

Table 1. Information of the CO_2 measuring sites used in this study.

Site code	Full name	Instrument	Lat. (° N)	Long. (° E)	AGL (m)	Mean daytime CO_2 concentration ± 1σ (ppm)
GWA	Gwanak Mountain	PICARRO G2401	37.443	126.967	231.004	446.2 (± 15.1)
NST_H	N Seoul Tower-High	Li-850	37.551	126.988	335.763	445.9 (± 11.8)
NST_L	N Seoul Tower-Low	PICARRO G2401	37.551	126.988	180.763	455.3 (± 22.8)
OLP	Olympic Park	PICARRO G2401	37.521	127.116	6.017	455.1 (± 20.4)
YSB	Yongsan Building	Li-850	37.523	126.963	97.717	477.4 (± 34.0)
SNU	Seoul National University	Li-850	37.463	126.956	28.380	462.9 (± 21.7)

In this study, only daytime observations (12:00–16:00 KST, 03:00–07:00 UTC) after December 3 were used for assimilation, considering the errors related to the nocturnal PBLH and the spin-up period of the atmospheric transport model. A total of 924 observations were used in the model. The distribution of the observed concentrations is shown in Fig. S1 of the Supplement.

https://doi.org/10.5194/egusphere-2026-5709
Preprint. Discussion started: 3 November 2026
© Author(s) 2026. CC BY 4.0 License.

2.2.2 Atmospheric Transport Model: WRF-STILT

A Stochastic time-inverted Lagrangian transport (STILT) model (Fasoli et al., 2018; Lin et al., 2003), coupled with weather research and forecasting (WRF) was used to generate footprint values. WRF-STILT has been widely used for urban-scale inverse modelling (Che et al., 2024; Kunik et al., 2019; Sim and Jeong, 2025). In WRF-STILT, particles are released from receptors based on WRF meteorological fields. By tracking particle trajectories, footprint values representing the sensitivity of concentrations at observation sites (receptors) to upwind surface fluxes are generated.

WRF meteorological fields were generated for December 2021 using a configuration similar to that described by Sim and Jeong (2025), with additional enhancements. Specifically, we added observation nudging and incorporated operational sea surface temperature and sea ice analysis (OSTIA) sea surface temperature (SST) data to enhance the accuracy of WRF simulations. Observation nudging included wind, temperature, and water vapor mixing ratio data from four Korea Meteorological Administration automated synoptic observation system (ASOS) sites located within the innermost WRF domain, domain 3 (information on domain 3 and the ASOS sites information is shown in Fig. S4 and Table. S1 in the Supplement, respectively). OSTIA SST fields were also used since they provide higher-resolution SST inputs and have been reported to demonstrate high accuracy over the Korean Peninsula (Xie et al., 2008; Lee et al., 2010; Mun et al., 2017). With these improvements, the simulated meteorological fields showed high agreement with the observed wind speed, wind direction, temperature, and relative humidity. The wind speed mean bias error was 0.87 m s^{-1}, and the index of agreement (IOA) and correlation coefficients (r) exceeded 0.74 across all four variables. Detailed descriptions of the WRF configuration and validation of the meteorological outputs against observations are provided in Text S1 of the Supplement.

For STILT, an ensemble of 1000 particles was released from each of the six receptor locations at the AGL of the measurement inlet and traced backward for 24 hours. In the inversion framework, these 24-hours backward footprint files were assembled into a Jacobian matrix (**H**) organized according to the temporal structure of the prior emissions. Since emission corrections were performed following this temporal structure, CO_2 enhancement at a single observation site contributed to updating emission estimates over the preceding 24-hour period, similar to four-dimensional data assimilation. A further explanation of the footprint calculations in STILT and the monthly averaged footprint values for the six sites can be found in Text S2 of the Supplement.

2.2.3 Biogenic CO_2 Fluxes

Urban CO_2 concentrations are influenced not only by anthropogenic emissions but also by biospheric activity. Considering these biospheric contributions, biogenic CO_2 fluxes ($\boldsymbol{s_{bio}}$) for December 2021 were obtained from the Carbon Simulator from Space (CASS). CASS is a data-driven terrestrial carbon flux that estimates net ecosystem exchange (NEE) using meteorological variables such as air temperature, humidity, photosynthetically active radiation (PAR), and satellite vegetation indices with coefficients optimized using a random-forest model. The biogenic NEE CO_2 fluxes utilized in this study encompassed the region from Seoul to Gyeonggi Province (Fig. 1a, outer domain). The spatiotemporal distributions of biogenic

https://doi.org/10.5194/egusphere-2026-5709
Preprint. Discussion started: 3 November 2026
© Author(s) 2026. CC BY 4.0 License.

CO_2 fluxes are shown in Fig. S7 of the Supplement. Within the Seoul domain, CASS showed relatively strong CO_2 uptake near the GWA region and northwest Seoul. In the outer domain, strong uptake was also evident in the northeastern region of Gyeonggi Province. The daytime NEE CO_2 fluxes over the domain were -2.8 ± 0.99 μmol CO_2 m^{-2} s^{-1}.

2.3 Methodologically Varied Inputs

2.3.1 Background Concentration

The observed atmospheric CO_2 concentrations ($\boldsymbol{z_{obs}}$) include contributions from local anthropogenic emissions as well as externally transported CO_2, reflecting atmospheric transport and mixing processes. To estimate the CO_2 enhancement attributable to anthropogenic emissions, it is essential to determine appropriate background concentrations ($\boldsymbol{z_{bg}}$) that exclude local emission influences for Seoul. Selecting an appropriate background is critical in inverse modeling, because lower background values can result in overestimated emissions for the region (Che et al., 2022; Pisso et al., 2019). Previous studies on urban CO_2 inversion have employed various methods to estimate background concentrations. Sim and Jeong (2025) provided a comprehensive overview of background treatment, including the use of upwind sites, designated background sites, and statistical definitions derived from each observation site. Other studies have also used clean air stations (Pisso et al., 2019), upwind concentrations estimated using atmospheric transport models (Hamilton et al., 2024), and boundary concentrations simulated using atmospheric transport models (Lian et al., 2023).

In this study, we estimated 12 background concentrations using 12 statistical methods. These methods used observations from high-altitude sites, representative global or regional background sites, and upwind sites assumed based on the modeled wind field in Seoul. We compared simulated enhancements from the prior ($\mathbf{H} \cdot \boldsymbol{s_p}$) with observed enhancements ($\boldsymbol{z}$) derived under 12 different background concentrations and selected 3 methods showing higher consistency between $\mathbf{H} \cdot \boldsymbol{s_p}$ and $\boldsymbol{z}$. The selected methods were as follows: (1) 5th percentile within a 24-hour window at each site (BC1); (2) daily minimum values at the central, high-altitude urban site NST_H (BC2); and (3) two-day moving average from the suburban, high-altitude site GWA (BC3). Further details regarding this sensitivity test are provided in Text S3 of the Supplement.

Each site exhibited different $\boldsymbol{z}$ values according to three different methods (Fig. 2). At the high-altitude sites GWA and NST_H, the enhancement values derived using BC1 were higher than BC3-derived enhancements, whereas all other sites showed the order BC2 > BC3 > BC1 (Fig. 2a). Although BC2 and BC3 yielded similar distributions and temporal patterns, the ΔCO_2 derived using BC1-derived exhibited distinct differences. BC1, which applies a statistical approach to each site, showed a narrower distribution, indicating lower variability and more stable background concentrations. This distinct BC1 pattern was particularly pronounced at the OLP and SNU sites. As shown in the daily timeseries in Fig. 2b, BC1 exhibited relatively stable temporal variability, whereas BC2 and BC3 showed similar temporal variations but weaker agreement with BC1, with correlation coefficients dropping to 0.34 at OLP and 0.65 at SNU.

https://doi.org/10.5194/egusphere-2026-5709
Preprint. Discussion started: 3 November 2026
© Author(s) 2026. CC BY 4.0 License.

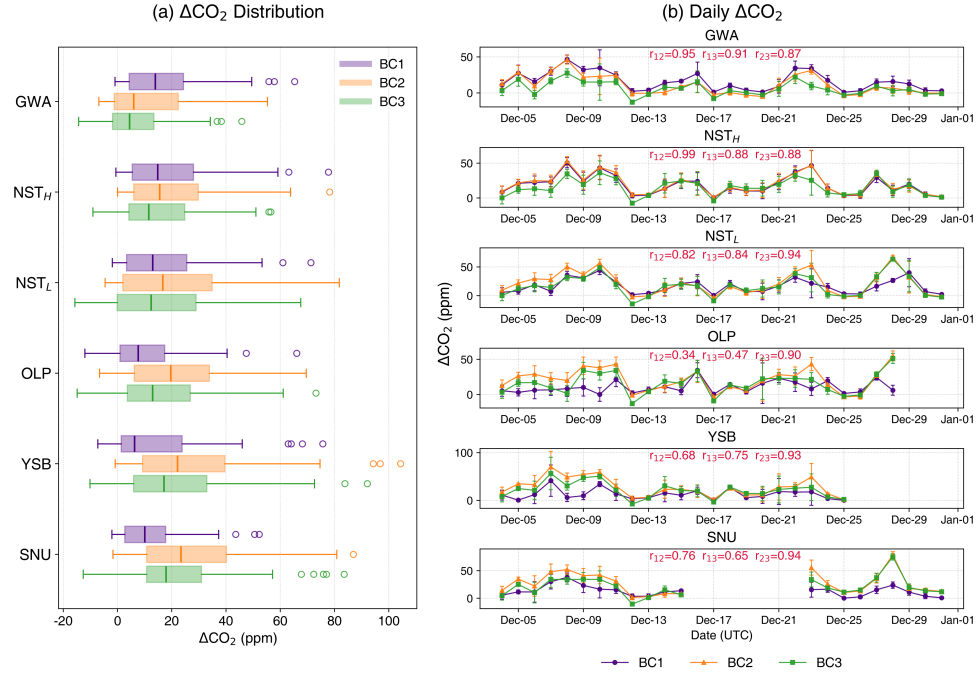


Figure 2. (a) Boxplots of ΔCO_2 at different observation sites under varying background concentrations and (b) time series of daily mean ΔCO_2 with error bars indicating daytime temporal variability (± 1 σ). Temporal correlation coefficients between different background concentrations are shown in red text; r_{12} (BC1 and BC2), r_{13} (BC1 and BC3), and r_{23} (BC2 and BC3).

2.3.2 Prior Emissions and Prior Error Covariance

In this study, fossil fuel CO_2 ($ffCO_2$) emission inventories served as the prior ($\boldsymbol{s_p}$) for inversions. We conducted inversions for Seoul using two distinct prior emissions data sets: the regional dataset of the Korea Carbon Project (KCP) and the global dataset ODIAC. The KCP v2025 datasets provides comprehensive estimates of carbon emissions (CO_2 and CH_4), sinks, and net flux for the Korean Peninsula. Region-specific emission inventories such as KCP have also been utilized for urban-scale inversions. For instance, the Hestia and Vulcan inventories have been used for U.S cities such as Boston (Sargent et al., 2018), Salt Lake City (Mallia et al., 2020), Indianapolis (Lauvaux et al., 2016), New York (Pitt et al., 2022), and the San Francisco Bay Area (Hamilton et al., 2024; Roten et al., 2023), as well as UNAM-EMI for Mexico City (Che et al., 2024), and Origins.Earth for Paris (Lian et al., 2022; Nalini et al., 2022). KCP $ffCO_2$ emissions are disaggregated into five sectors: "Power generation," "Buildings," "Manufacturing," "Transportation (On-road)," and "Transportation (Airport)." Sector-specific emissions at the administrative district level are estimated using domestic activity data and the highest tier methodology. The higher spatial resolution (0.01°) emissions are produced through spatial allocation proxies. In this study, we used KCP anthropogenic CO_2 data for December 2021 at 1 hour temporal and 0.01° spatial resolutions. We also employed ODIAC version 2022 (Oda et al., 2018; Oda and Maksyutov, 2011). ODIAC has been widely adopted in urban-scale studies of cities, including Indianapolis, Mexico City, Salt Lake City, Tokyo, Beijing, Riyadh, and Paris (Cai et al., 2025; Che et al., 2022; Che

https://doi.org/10.5194/egusphere-2026-5709
Preprint. Discussion started: 3 November 2026
© Author(s) 2026. CC BY 4.0 License.

et al., 2024; Kunik et al., 2019; Lian et al., 2022; Mallia et al., 2020). ODIAC integrates bottom-up fossil fuel carbon emission data from CDIAC, point source information from the CARMA database, and spatial allocation using satellite-based nighttime light data as spatial proxies (Oda et al., 2018). Previous studies have manually corrected the locations of point sources due to their occasional misallocation in ODIAC (Kunik et al., 2019; Ohyama et al., 2023; Sim and Jeong., 2025). ODIAC includes two major point sources along Seoul: the Danginri Power Plant operated by Korea Midland Power Co., Ltd. (KOMIPO) and the Korea District Heating Corporation Gangnam Branch. However, their geolocations in ODIAC deviate from their actual locations; therefore, we manually relocated these point sources, as shown in Fig. S8 of the Supplement. Since ODIAC provides monthly data at 1 × 1 km^2, we applied temporal downscaling using hourly and weekly scaling factors from Nassar et al. (2013).

For the daytime period in December, KCP showed a mean emission (± 1σ) of 37.1 (± 51.06) μmol CO_2 m^{-2} s^{-1}, while ODIAC exhibited slightly lower values of 35.0 (± 38.94) μmol CO_2 m^{-2} s^{-1}. Total daytime emissions were also higher for KCP at 624.7 Gg CO_2 compared to 590.2 Gg CO_2 of ODIAC. Fig. 3 presents the spatiotemporal distribution of prior emissions from KCP and ODIAC. KCP allocates emissions over the Han River to account for road transport emissions from bridges crossing it. ODIAC, however, does not consider emissions over water bodies, as indicated by the absence of emissions over the Han River (Fig. 3b). KCP also includes more than two point-sources, resulting in greater spatial heterogeneity in the emission distribution (Fig. 3a). The monthly averaged daytime emission differences between the two priors (Fig. 3c) revealed that KCP allocates higher emissions over the Han River area, exceeding 40 μmol CO_2 m^{-2} s^{-1}. KCP generally showed higher emissions, except in regions influenced by biogenic fluxes (Fig. S7). Figure 3d shows the daily averaged timeseries for both priors for December 2021. KCP exhibited a continuous increasing trend with variations ranging from 10 to 45 μmol CO_2 m^{-2} s^{-1}. ODIAC employs temporal proxies to allocate hourly variability, yielding more consistent temporal variation with a narrower range of 20–40 μmol CO_2 m^{-2} s^{-1}. Both priors demonstrated similar day of week variations, with lower emissions on weekends. However, KCP showed varying values for the same day of the week depending on the period within the month.

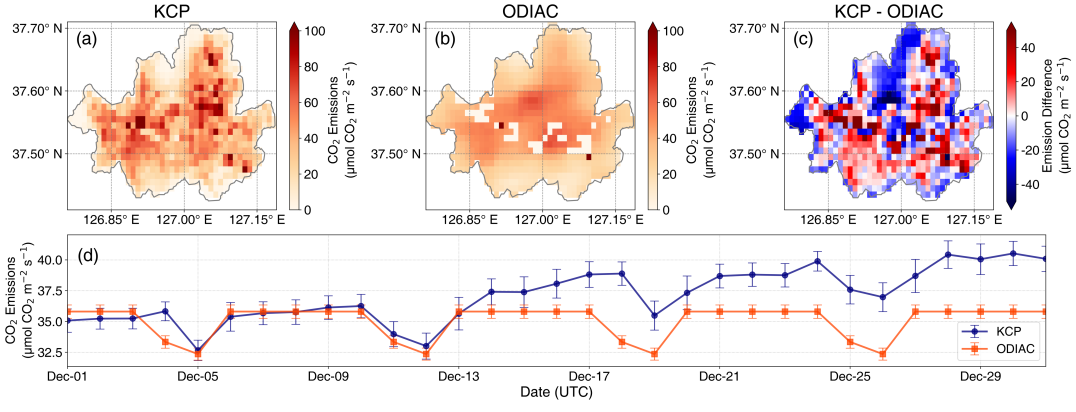


Figure 3. Spatial distribution and time series of daytime-averaged prior emissions from KCP and ODIAC over Seoul in December 2021. (a–c) Monthly mean spatial distributions: (a) KCP; (b) ODIAC; and (c) difference (KCP − ODIAC). (d) Time series of daily mean emissions with error bars indicating daytime temporal variability (± 1 σ) for KCP (blue) and ODIAC (orange).

https://doi.org/10.5194/egusphere-2026-5709
Preprint. Discussion started: 3 November 2026
© Author(s) 2026. CC BY 4.0 License.

The prior error covariance (**Q**) assumes uncertainties that account for the spatiotemporal heterogeneity of prior emissions. The matrix **Q** is composed of the prior uncertainty (σ), temporal covariance (**D**), and spatial covariance (**E**) using the Kronecker product, shown in Eq. (5) (Yadav and Michalak, 2013):

$$\mathbf{Q} = \mathbf{I}_\sigma(\mathbf{D}\otimes\mathbf{E})\mathbf{I}_\sigma \quad (5)$$

Here, I_σ is the diagonal matrix of the prior uncertainty (σ). Both the temporal (**D**) and spatial (**E**) covariance structures follow the exponential decay equations in Eq. (6) and Eq. (7):

$$\mathbf{D} = \exp(-\frac{\boldsymbol{X}_\tau}{l_\tau}) \quad (6)$$

$$\mathbf{E} = \exp(-\frac{\boldsymbol{X}_s}{l_s}) \quad (7)$$

Where $\boldsymbol{X}_\tau$ denotes the time difference between time steps and $\boldsymbol{X}_s$ represents the separation distance between grid cells. These are divided by the temporal correlation range parameter (l_τ) and the spatial correlation range parameter (l_s), respectively. Although the method for estimating the prior error covariance remains consistent across configurations, its values differ because the underlying prior datasets are different. Specifically, the two prior datasets, KCP and ODIAC, have different uncertainties. KCP provides uncertainty estimates, with a mean uncertainty-to-emission ratio of 13.9 % for December 2021. For ODIAC, we assigned relative uncertainties of 15 % to point sources and 85 % to all other areas within Seoul, following Ohyama et al. (2023). Grid cells containing the Han River were allocated a minimum uncertainty of 1 μmol CO_2 m^{-2} s^{-1}, adopting the approach followed by Kunik et al. (2019) and Sim and Jeong (2025). The resulting mean uncertainty of the emission ratio for ODIAC was 84.7 %, which is approximately eight times larger than that of KCP. The detailed spatiotemporal variability of these uncertainties is presented in Text S4.1 of the Supplement. The spatial and temporal correlation range parameters were also set separately for each prior, because these parameters depend on the target city and emission dataset. Following Kunik et al. (2019) and Sim and Jeong (2025), we estimated l_τ using the lagged autocorrelation function and l_s using variogram analysis, as described in Text S4.2 of the Supplement. Based on these analyses, l_τ and l_s were set to 5 h and 7 km for KCP, and 9 h and 10 km for ODIAC, respectively.

2.3.3 Observation Error Covariance

The observation error covariance (**R**), also referred to as the model-data mismatch error represents uncertainties derived from both observations and transport models (Kunik et al., 2019; Stohl et al., 2009). Recent studies have employed various approaches to estimate the matrix **R**, with most adopting a diagonal matrix **R** as the summation of different uncertainty sources. The sources vary considerably in previous studies. For example, Vardag and Maiwald (2024) composed **R** as the sum of the instrument, representation, and transport model errors. Jones et al. (2021) and Hamilton et al. (2024) considered the background, instrument, transport, and source distribution errors. More comprehensive sources have been considered in studies of Salt Lake

https://doi.org/10.5194/egusphere-2026-5709
Preprint. Discussion started: 3 November 2026
© Author(s) 2026. CC BY 4.0 License.

City, typically accounting for errors related to the finite number of particles, vertical and horizontal wind transport, background concentrations, biospheric flux, and grid cell aggregation (Kunik et al., 2019; Mallia et al., 2020; Mallia et al., 2023). Additionally, certain studies have incorporated temporal and spatial correlation structures into the matrix **R** using double exponential decay functions applied to these summed error terms. For instance, studies in the Los Angeles Basin considered various errors (e.g., instrument, stochastic, and PBL errors) and subsequently applied exponential decay terms (Roten et al., 2022). Similarly, in New York, measurement, model, and background errors were considered with correlation length scales of 1 km and 1 h, as reported for atmospheric trace gases in urban environments (Pitt et al., 2022). The matrix **R** has also been estimated by indirect methods. For Tokyo, **R** was estimated using the relative residual error method suggested by Heald et al., (2004). which computes the matrix **R** using the relative residual standard deviation between simulated and observed ΔCO_2 (Ohyama et al., 2023). Diagnostic methods have also been adopted in previous studies. Sim and Jeong. (2025) used the Hollingsworth-Lönnberg method (Hollingsworth and Lönnberg, 1986; Rutherford, 1972). Bréon et al. (2015) specified **R** as a diagonal matrix with a value of 3 ppm, determined using a diagnostic method following Desroziers et al. (2005). Alternatively, other studies have incorporated spatial gradients between observation sites. Lian et al. (2021) allocated consistent **R** values, differentiated for urban-suburban and suburban-suburban pairs, within a diagonal matrix.

In this study, we employed three commonly used assumptions for estimating observation error: (1) the relative residual error method (Rres; Heald et al., 2004; Ohyama et al., 2023), (2) the uncertainty summation method (Rsum; Mallia et al., 2020), and (3) the diagnostics method (RDx; Desroziers et al., 2005). Detailed descriptions of these three methods and their applications in the Seoul inversion framework are provided in Text S5 of the Supplement.

Since the estimation of **R** depends on both the prior emissions and background concentration methods, combining two prior emissions with three background approaches yields six distinct model configurations, each producing different matrix **R** values despite using the same observation error estimation method. Figure 4 presents the diagonal elements of **R** averaged over the six configurations ($n \times 1$). The standard deviation shown in Fig. 4a reflects both the variability across the six configurations and the temporal fluctuations at each observation site. Across all sites, mean **R** values followed the order Rres > RDx > Rsum. The standard deviations of Rres and Rsum include temporal fluctuations at each site, whereas RDx assumes temporally constant observation errors. Thus, the standard deviation of RDx represents only the variability across the six configurations and is particularly large at OLP, YSB, and SNU. All three methods assigned the largest observational errors to YSB, a site strongly influenced by emissions. Figure 4b illustrates the temporal variability. The Rres method is proportional to $\boldsymbol{z}_{obs}$ and therefore exhibits larger fluctuations than the other methods. This approach assigns higher errors to larger concentration enhancements and lower errors to smaller enhancements. In contrast, Rsum shows highly stable temporal variability. The weak temporal correlation of 2.8 h assigned to $\mathbf{R}_{transwind}$ and the 1.5 % uncertainty based on the observed concentrations at NST_H, YSB, and SNU (which use Li-850) resulted in slightly stronger temporal correlations than those at sites using PICARRO sensors (Fig. S12). RDx remained constant throughout the period owing to its inherent assumption of no temporal variability.

https://doi.org/10.5194/egusphere-2026-5709
Preprint. Discussion started: 3 November 2026
© Author(s) 2026. CC BY 4.0 License.



Figure 4. (a) Mean diagonal elements of R and their standard deviation at each site under three different observation error assumptions. (b) Time series of daily mean diagonal elements of R, with error bars indicating daytime temporal variability (± 1 σ) at each site. All values are averaged across six inverse modeling configurations: two prior emission inventories (KCP and ODIAC) and three background concentrations (BC1, BC2, and BC3).

2.4 Study Design

We constructed 18 inversion cases by combining two prior inventories (KCP and ODIAC), three background concentration methods (BC1, BC2, and BC3), and three observation error covariance assumptions (Rres, Rsum, and RDx), as summarized in Table 2. These cases were used to estimate the ffCO_2 emissions over Seoul in December 2021. We analyzed the estimates only during the daytime, considering errors related to the transport model.

Table 2. List of the inversion configurations.

Inversion case	Prior Emissions	Background Concentrations	Observation Error
KCP_BC1_Rres	KCP	BC1	Rres
KCP_BC1_Rsum	KCP	BC1	Rsum
KCP_BC1_RDx	KCP	BC1	RDx
KCP_BC2_Rres	KCP	BC2	Rres
KCP_BC2_Rsum	KCP	BC2	Rsum
KCP_BC2_RDx	KCP	BC2	RDx

https://doi.org/10.5194/egusphere-2026-5709
Preprint. Discussion started: 3 November 2026
© Author(s) 2026. CC BY 4.0 License.

KCP_BC3_Rres	KCP	BC3	Rres
KCP_BC3_Rsum	KCP	BC3	Rsum
KCP_BC3_RDx	KCP	BC3	RDx
OD_BC1_Rres	ODIAC	BC1	Rres
OD_BC1_Rsum	ODIAC	BC1	Rsum
OD_BC1_RDx	ODIAC	BC1	RDx
OD_BC2_Rres	ODIAC	BC2	Rres
OD_BC2_Rsum	ODIAC	BC2	Rsum
OD_BC2_RDx	ODIAC	BC2	RDx
OD_BC3_Rres	ODIAC	BC3	Rres
OD_BC3_Rsum	ODIAC	BC3	Rsum
OD_BC3_RDx	ODIAC	BC3	RDx

2.4.1 Intercomparison of 18 Inversion Cases

To assess the impact of different assumptions on the estimates, we compared 18 inversion results, focusing on the total fluxes, temporal variability, and spatial distribution of posterior emissions. The performance of each inversion case was further evaluated by comparing the simulated ΔCO_2 from prior ($\mathbf{H} \cdot \boldsymbol{s}_p$) and posterior fluxes ($\mathbf{H} \cdot \hat{\boldsymbol{s}}$) with observed ΔCO_2 ($\boldsymbol{z}$).

Based on the 18 inversion results, we compared the contributions of the different assumptions applied to each input (prior emissions, background concentrations, and observation error covariances) to the posterior emission estimates. For total fluxes, and the analysis of variance (ANOVA) was conducted to assess which parameter assumptions exerted a greater effect on changes in total emissions. Effect sizes were quantified using partial eta squared ($\eta_p{}^2$), representing the proportion of variance in posterior emissions explained by each parameter assumption (Lakens, 2013). For the temporal variability and spatial distribution of posterior emissions, similarity among the estimates was quantified using correlation coefficients (r). Correlations between inversion pairs sharing the same assumption were compared with those derived from different assumptions, and a paired t-test was applied to assess which input assumptions caused larger changes in temporal variability and spatial distribution. Effect sizes for the paired comparisons were evaluated using "Relative Change" (%) to quantify the magnitude of changes in similarity, and Cohen's d_z to assess the consistency of parameter influence across inversion cases (Cohen, 1988; Lakens, 2013).

Both ANOVA and paired t-tests were conducted primarily considering the main effects of each parameter. Interaction effects were also examined as supplementary diagnostics to assess whether the influence of one parameter assumption depended on the configuration of another. Because the number of inversion configurations was limited (N = 18) and the inversion cases were not fully independent, as multiple configurations shared common inputs and configurations, statistical significance was interpreted with caution. Therefore, p-values were used only as reference indicators and the relative influence of each parameter

https://doi.org/10.5194/egusphere-2026-5709
Preprint. Discussion started: 3 November 2026
© Author(s) 2026. CC BY 4.0 License.

was evaluated primarily based on effect size. Detailed methods for the ANOVA and paired t-tests including definitions of the statistical metrics are provided in Text S6 of the Supplement.

2.4.2 Parameter Sensitivity

To quantify the uncertainty arising from different assumptions, we defined parameter sensitivity as the deviation in posterior estimates resulting from the choice of parameter assumptions. For each of the 18 model configurations, we identified a corresponding group of 6 configurations to calculate this sensitivity. This group includes the baseline configuration itself and five variations derived by changing only one parameter at a time. Given our experimental design (two priors, three background concentrations, and three observation errors), this group comprises the baseline, one case with a different prior, two cases with different backgrounds, and two cases with different observation errors.

Parameter sensitivity was calculated using Eq. (8), based on the definition of posterior uncertainty in different inversions by Zhang et al. (2024), where it is provided as the standard deviation of estimates across different inversions.

$$Parameter\ Sensitivity = \sqrt{\frac{1}{6} \times \sum_{i=1}^{6} (x_i - \mu)^2} \quad (8)$$

Where x_i represents the emission value for the ith configuration in the subset, and μ is the mean of these six estimates. We quantified parameter sensitivity across the 18 inversion cases as described in Section 3.3 and derived robust emission estimates for Seoul considering the parameter sensitivity described in Section 3.4. The contribution of each assumption to the sensitivity was estimated from the standard deviation across the results obtained by varying the prior emissions, background concentrations, and observation errors.

2.4.3 Uncertainty Reduction Ratio

Finally, we examined whether the divergence between the posterior estimates under different assumptions surpassed the divergence of prior emissions. If the posterior discrepancies exceed those of the priors, the inversion system may not effectively constrain the fluxes, indicating limited robustness of the inversion system to different methodological assumptions. To evaluate this performance, we computed the Uncertainty Reduction Ratio (URR) by adopting an approach similar to that of Zhang et al. (2024), as defined in Eq. (9):

$$URR = -\ln\left(\frac{\sigma_{posteriors}}{\sigma_{priors}}\right) \quad (9)$$

Where σ_{priors} denotes the standard deviation between two priors (KCP and ODIAC), and $\sigma_{posteriors}$ represents the standard deviation of posterior estimates.

https://doi.org/10.5194/egusphere-2026-5709
Preprint. Discussion started: 3 November 2026
© Author(s) 2026. CC BY 4.0 License.

3 Results

3.1 Intercomparison of 18 Posterior Estimates

The summarized results from the 18 inversion cases are listed in Table 3, including the mean and total daytime posterior CO_2 emissions, mean daytime posterior uncertainties, the agreement between posterior-simulated CO_2 enhancements ($\Delta CO_{2,mod}$) and observed CO_2 enhancements ($\Delta CO_{2,obs}$), and the prior-to-posterior emission changes.

Table 3. Comparison of inversion results across different inversion configurations. The table presents the mean and total daytime posterior CO_2 emissions, the relative change in total emissions, mean daytime posterior uncertainties, and observation-space performance metrics for the 18 posterior cases, including the Pearson correlation coefficient (r) and Mean Absolute Error (MAE) between $\Delta CO_{2,\,mod}$ and $\Delta CO_{2,\,obs}$. The change in total emissions (%) was calculated as ((Total posterior – Total prior) ×Total prior^{-1} ×100 %). The correction magnitude represents the sum of absolute emission changes ((∑|posterior-prior|)×(∑prior)$^{-1}$×100 %).

Inversion case	Mean daytime CO_2 emissions (μmol $m^{-2}s^{-1}$)	Total daytime CO_2 emissions (Gg CO_2)	Change in total emissions (%)	Mean daytime posterior uncertainty (μmol $m^{-2}s^{-1}$)	Correlation coefficient (r)	MAE (± 1 σ)	Correction Magnitude (%)
KCP_BC1_Rres	23.49	395.68	-36.66	1.98	0.33	11.7 (± 12.9)	36.7
KCP_BC1_Rsum	33.97	572.22	-8.40	2.32	0.31	11.7 (± 10.7)	9.9
KCP_BC1_RDx	35.23	593.31	-5.02	2.33	0.27	12.1 (± 11.4)	6.5
KCP_BC2_Rres	30.93	520.85	-16.62	2.22	0.56	13.2 (± 13.9)	17.4
KCP_BC2_Rsum	35.61	599.72	-4.99	2.35	0.60	12.8 (± 12.4)	6.4
KCP_BC2_RDx	37.16	625.89	+0.19	2.36	0.56	13.0 (± 12.8)	4.7
KCP_BC3_Rres	30.85	519.64	-16.81	2.25	0.51	11.8 (± 11.9)	17.0
KCP_BC3_Rsum	34.66	584.01	-6.51	2.33	0.56	11.3 (± 10.7)	8.7
KCP_BC3_RDx	36.29	611.17	-2.16	2.36	0.49	12.0 (± 11.6)	5.1
OD_BC1_Rres	22.80	383.98	-34.94	9.62	0.47	10.5 (± 12.1)	42.0
OD_BC1_Rsum	31.30	527.10	-10.69	10.99	0.61	9.1 (± 9.6)	36.6
OD_BC1_RDx	34.59	582.56	-1.30	10.13	0.65	8.1 (± 9.3)	39.8
OD_BC2_Rres	31.11	523.93	-11.23	10.24	0.70	11.2 (± 12.8)	38.5
OD_BC2_Rsum	37.16	625.92	+6.05	11.34	0.79	10.3 (± 10.2)	33.7
OD_BC2_RDx	41.78	703.70	+19.23	10.68	0.81	8.7 (± 9.2)	45.6
OD_BC3_Rres	24.54	413.36	-29.96	10.41	0.64	10.5 (± 11.9)	38.4
OD_BC3_Rsum	34.09	574.12	-2.73	11.04	0.78	9.1 (± 8.6)	38.9
OD_BC3_RDx	36.70	618.18	+4.74	10.64	0.80	8.0 (± 8.0)	45.7

https://doi.org/10.5194/egusphere-2026-5709
Preprint. Discussion started: 3 November 2026
© Author(s) 2026. CC BY 4.0 License.

Compared with the prior total daytime CO_2 emissions (624.7 Gg CO_2 for KCP and 590.2 Gg CO_2 for ODIAC), 11 of the 18 posterior estimates showed lower total emissions than both prior CO_2 emissions. In contrast, three cases (KCP_BC2_RDx, OD_BC2_Rsum, and OD_BC2_RDx) exceeded the KCP totals, whereas four cases (KCP_BC1_RDx, KCP_BC2_Rsum, KCP_BC3_RDx, and OD_BC3_RDx) fell between the two priors. When grouped by background concentration assumptions, total emissions showed a consistent pattern across all 18 results, with the cases using BC2 yielding the highest total emissions, followed by those using BC3 and BC1. This tendency was consistent with the comparison of $\boldsymbol{z}$ under different background assumptions (Section 2.3.1) suggesting that background concentration determines the emission level, as proposed in previous studies (Che et al., 2022; Pisso et al., 2019). Additionally, analysis using the observation error method revealed that cases employing the Rres method estimated substantially lower emissions than the other methods. This can be explained by the Rres assumption method which calculates observation errors proportionally to $\boldsymbol{z}$, thereby assigning smaller errors to lower values of $\boldsymbol{z}$ and resulting in greater assimilation of low-$\boldsymbol{z}$ values.

The daily daytime averaged timeseries of prior and posterior emissions over Seoul from the 18 different inversion cases are illustrated in Fig. 5. All 18 posterior time series exhibited greater variability than their respective priors. Notably, cases using the same observation error assumption showed similar temporal fluctuations. The contribution of each parameter to these temporal variability patterns is quantified in Section 3.2. The posterior time series generally fluctuated between 10 and 50 μmol CO_2 m^{-2} s^{-1}, with distinct decreases on December 23 and increases on December 29 consistently appearing across all 18 inversions. Notably, the magnitude of the December 29 peak varied among configurations, reaching more than 80 μmol CO_2 m^{-2} s^{-1} in inversion cases that combined the ODIAC prior with the Rsum or RDx observation error assumptions.

https://doi.org/10.5194/egusphere-2026-5709
Preprint. Discussion started: 3 November 2026
© Author(s) 2026. CC BY 4.0 License.

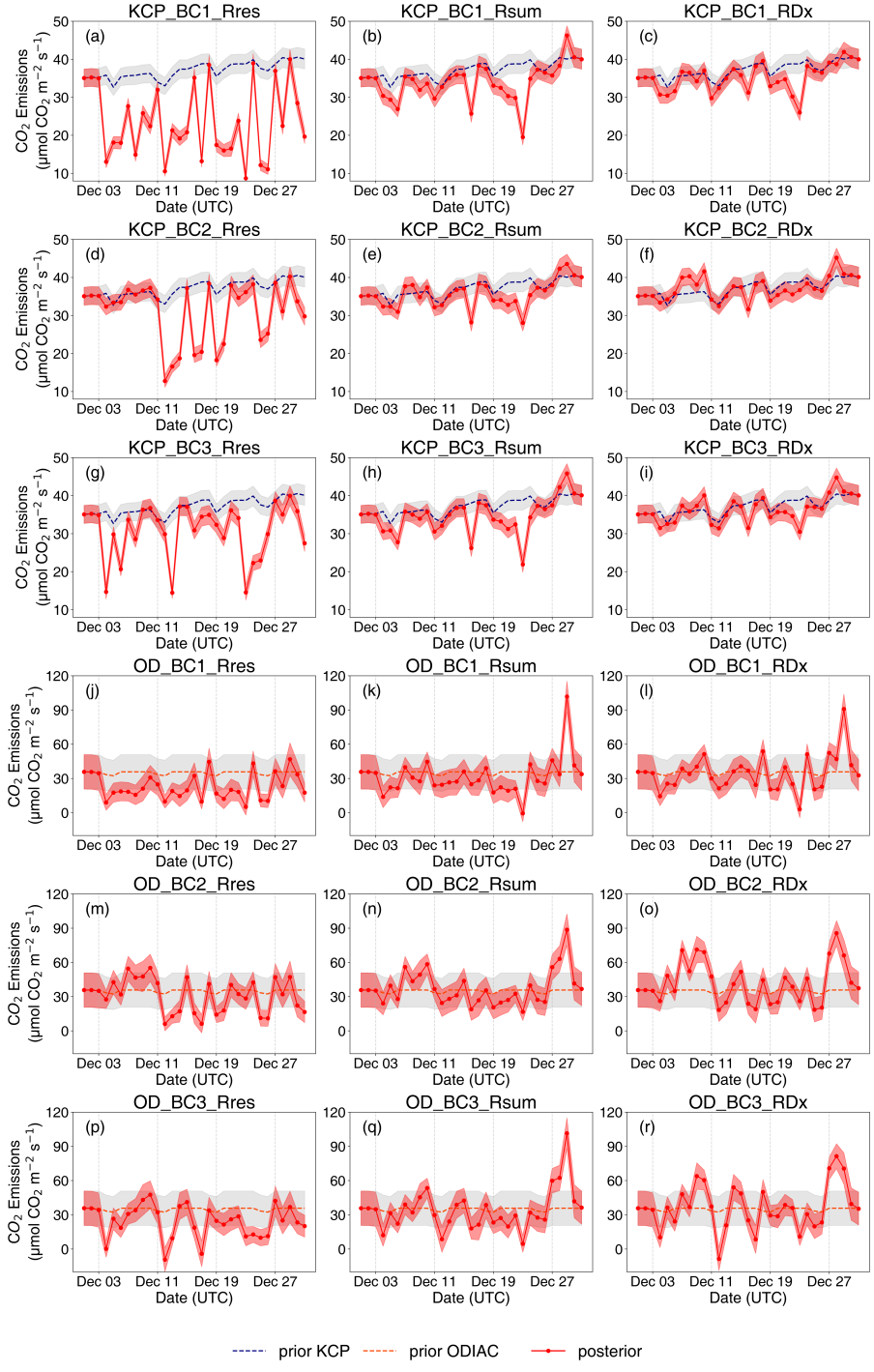


Figure 5. Time series of daytime (3:00-7:00 UTC) daily domain-averaged emissions comparing prior (navy for KCP, orange for ODIAC) with posterior (red) estimates. Emission uncertainties are shown as shaded regions in gray (prior) and red (posterior). Note

https://doi.org/10.5194/egusphere-2026-5709
Preprint. Discussion started: 3 November 2026
© Author(s) 2026. CC BY 4.0 License.

that the y-axis ranges differ between panels: 0–50 µmol CO_2 m^{-2} s^{-1} for posterior estimates using the KCP prior ((a)–(i)), and −20 to 120 µmol CO_2 m^{-2} s^{-1} for those using the ODIAC prior ((j)–(r)).

Figure S13 shows a comparison of the spatial distribution across the 18 monthly averaged daytime emissions over Seoul. The spatial distribution of the posterior emissions was predominantly affected by information from the priors. Further exploration of the monthly averaged spatial distribution of the posterior-prior emission correction was conducted, as shown in Fig. 6. All 18 correction maps showed that the correction magnitude was proportional to the emission levels, because the prior uncertainty was scaled with the prior emission levels. Most of the 18 cases exhibited emission reductions across Seoul. However, several cases exhibited a more complex spatial correction pattern, with reductions in the eastern part of Seoul and increases in the western part. This pattern was more distinct in cases using ODIAC as the prior than in those using KCP.

https://doi.org/10.5194/egusphere-2026-5709
Preprint. Discussion started: 3 November 2026
© Author(s) 2026. CC BY 4.0 License.

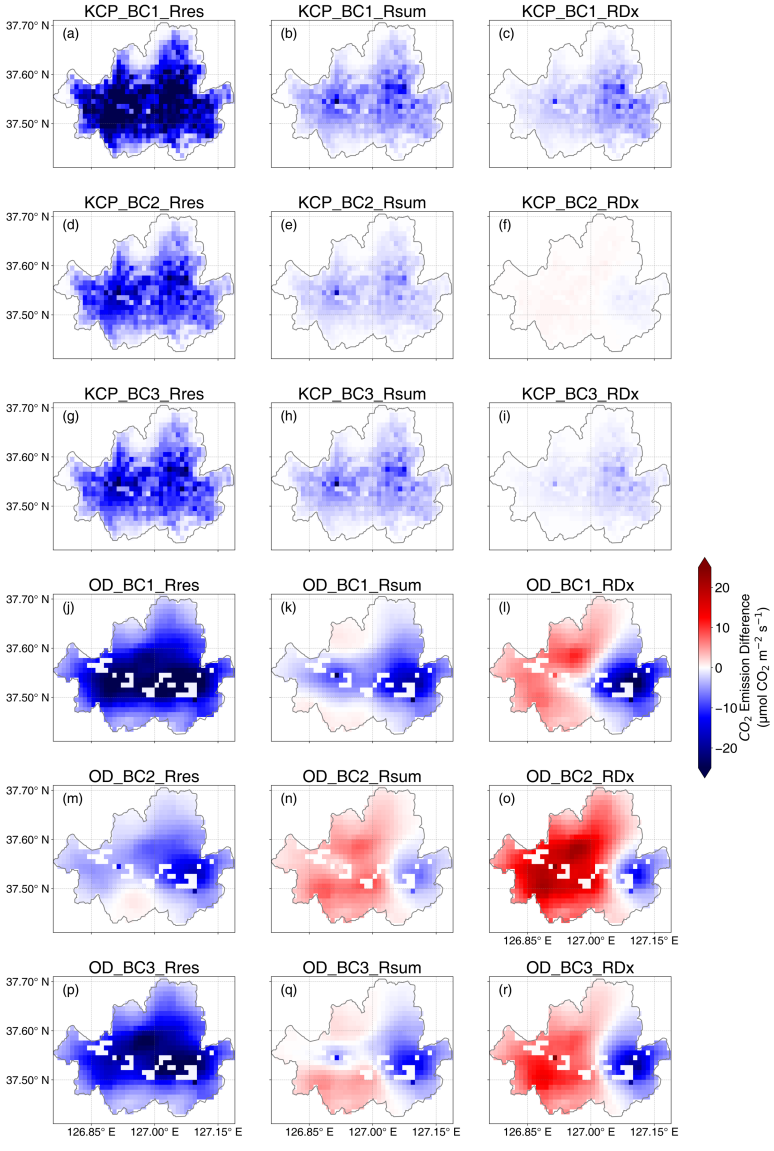


Figure 6. Daytime (3:00-7:00 UTC) emission correction maps (posterior-prior) for the 18 inversion configurations.

The posterior uncertainties decreased across all 18 cases compared to the prior emission uncertainties of 2.45 μmol CO_2 m^{-2} s^{-1} for KCP and 14.75 μmol CO_2 m^{-2} s^{-1} for ODIAC. As shown in Table 3, cases using KCP showed a smaller uncertainty reduction, which can be attributed to the lower prior uncertainty, resulting in less correction from observation compared to cases using ODIAC. However, even after inverse modeling, the posterior uncertainties using KCP remained lower than those using ODIAC. To evaluate whether the posterior CO_2 estimates were well constrained by the observations, we compared the observed CO_2 enhancement ($\Delta CO_{2,obs}$) with the CO_2 enhancements simulated using the prior emissions and the 18 posterior emission estimates ($\Delta CO_{2,mod}$). Table 3 presents the correlation coefficient (r) and mean absolute error (MAE) between ΔCO_2,

https://doi.org/10.5194/egusphere-2026-5709
Preprint. Discussion started: 3 November 2026
© Author(s) 2026. CC BY 4.0 License.

$_{obs}$ and $\Delta CO_{2,mod}$ for the 18 posterior cases. A comparison with the prior simulations, along with additional performance metrics including the RMSE, IOA, and r, is provided in Fig. S14, while the MAE with ± 1σ is shown in Fig. S15 of the Supplement. In all cases, the posterior simulations showed improved agreement with the observations than the prior simulations did. The posterior cases using ODIAC generally demonstrated higher consistency with the observations after inversions, owing to the higher assimilation magnitude of observation data. However, considering configurations with similar agreement performance can reveal completely different spatial distributions of emissions estimates, depending on the choice of prior emissions, as shown in Fig. S13 of the Supplement. Therefore, the selection of optimal emissions should consider multiple factors beyond consistency with observations, including the spatiotemporal characteristics of the posterior estimates and their uncertainties.

3.2 Influence of Parameter Assumptions on Posterior Emissions

To identify the selective impact of parameter assumptions on posterior emissions, we quantified the contribution of parameter assumptions to the total amount, temporal variability, and spatial distribution across the 18 posterior emissions as summarized in Table 4.

Table 4. Main statistical effects of parameter assumptions on posterior emissions.

Information aspect	Parameter	Effect size (η_p^2)	F	p
Total emissions	Prior emissions	0.02	0.25	0.627
	Background concentration	0.66	11.43	0.002
	Observation error	0.87	39.62	< 0.001
		Relative change (%)	Cohen's d_z	p
Temporal variability	Prior emissions	19.69	0.52	0.043
	Background concentrations	20.78	1.07	< 0.001
	Observation error	34.51	1.40	< 0.001
Spatial distribution	Prior emissions	31.95	11.26	< 0.001
	Background concentrations	-2.30	-2.43	< 0.001
	Observation error	-1.39	-1.36	< 0.001

The ANOVA results indicated that the total posterior emissions were strongly influenced by the choice of observation error assumption (F = 39.6, p < 0.001). This factor explains 87 % of the variance in total posterior emissions (η_p^2 = 0.87), representing a dominant source of variability. The background concentration method also exhibited a statistically significant effect (F = 11.4, p = 0.002), with a substantial effect size (η_p^2 = 0.66), explaining 66 % of the variance in total posterior emissions. In contrast, the choice of prior inventory assumption did not yield a statistically supported difference (p = 0.63), and its associated effect size was negligible (η_p^2 = 0.02). These results are consistent with the patterns described in Section

https://doi.org/10.5194/egusphere-2026-5709
Preprint. Discussion started: 3 November 2026
© Author(s) 2026. CC BY 4.0 License.

3.1. Additionally, a two-way interaction ANOVA showed no evidence of interactions among prior emissions, background concentrations, and observation error assumptions (Table S8 of the Supplement, all $p > 0.1$). In estimating the total emissions over Seoul, assumptions regarding observation error and background concentration were the dominant drivers of variability, with observation error assumptions exerting the strongest influence. However, differences between prior inventories did not result in detectable variations in total posterior emissions, likely because the difference in total emissions between the prior datasets was small compared with the range of posterior corrections across the inversion cases in this study.

The similarity in temporal variability among posterior emission estimates was higher when observation error assumptions were identical (mean $\bar{r}^{same} = 0.68$) than when they differed (mean $\bar{r}^{diff} = 0.52$), an increase of 34.5 % relative to different assumptions ($p < 0.001$). Using the same background concentration method also increased the similarity in temporal emission variability by 20.8 % ($\bar{r}^{same}$-$\bar{r}^{diff} = 0.096$, $p < 0.001$), and using the same prior inventory resulted in an average increase of 19.7 % ($p < 0.05$). However, Cohen's d_z values differed substantially among factors: 1.40 for observation error, 1.07 for background concentration, and 0.52 for prior data. These results indicate that although the choice of prior influenced temporal variability on average, its effect was less consistently expressed across inversion cases. In contrast, the observation error and background concentration assumptions produced more consistent responses, suggesting that the temporal variability of posterior estimates was more sensitive to these assumptions than to the choice of prior inventory. Interaction analysis revealed a significant interaction between the prior and background concentration assumptions, indicating their joint influence on the temporal variability of the posterior depended on their combined configuration (Table S8). However, the effect size and its consistency were weaker than those of the main effects.

Notably, the similarity in the spatial distribution among the posterior was predominantly controlled by the choice of prior. Spatial correlation between inversion cases using the same prior was substantially higher (mean $\bar{r}^{same} = 0.97$) than that using different priors (mean $\bar{r}^{diff} = 0.73$), corresponding to a 31.9 % increase ($\Delta r = 0.23$, $p < 0.001$). This effect was highly consistent across inversion cases, as indicated by the exceptionally large Cohen's d_z value of 11.26. In comparison, the background concentration and observation error assumptions showed minimal influence on spatial similarity, with absolute relative changes of only 2.3 % and 1.4 %, respectively. These results highlight the dominant role of prior spatial information in shaping the spatial structure of posterior emission estimates. Additional interaction analyse revealed a significant interaction between the background concentration method and observation error assumptions (Table S8), indicating that different combinations of background concentration and observation error assumptions influenced the spatial distribution of posterior emissions. However, the role of prior emissions remained dominant, as the spatial distribution of the posterior was overwhelmingly controlled by the prior employed. Detailed results of the interaction analysis are summarized in Table S8 of the Supplement.

3.3 Parameter Sensitivity

We quantified the parameter sensitivities for each of the 18 inversion cases to evaluate the uncertainty in posterior estimates arising from different parameter assumptions. Figure 7a shows the total magnitude across the 18 parameter sensitivities for

https://doi.org/10.5194/egusphere-2026-5709
Preprint. Discussion started: 3 November 2026
© Author(s) 2026. CC BY 4.0 License.

daytime emissions in December 2021, along with the contribution of each assumption and the uncertainties in both the prior and posterior estimates. Across all 18 cases, parameter sensitivity consistently exceeded posterior uncertainty. This indicates that the posterior uncertainty from an individual case cannot fully represent the uncertainty from different parameter assumptions. Parameter sensitivity was also larger than the KCP prior uncertainty, but smaller than the ODIAC prior uncertainty. Total parameter sensitivity ranged from a minimum of 151.2 Gg CO_2 (KCP_BC3_Rsum) to a maximum of 222.6 Gg CO_2 (OD_BC1_RDx). Regarding prior emission assumptions, cases using KCP exhibited parameter sensitivities of 151–157 Gg CO_2, whereas ODIAC based cases showed higher sensitivities of 194 –223 Gg CO_2. With respect to the background concentration methods, no distinct patterns were indicated. For observation error assumptions, the cases using Rsum showed the lowest sensitivity, while Rres and RDx cases exhibited similar levels. The ratio of total parameter sensitivities to total emission estimates ranged from 25.6 % to 51.5 %. Inverse modelling setups with lower parameter sensitivity yield posterior emissions that are less sensitive to variations in input parameter assumptions, indicating greater statistical robustness. Therefore, estimates with lower parameter sensitivities were considered when deriving the robust estimates for Seoul.

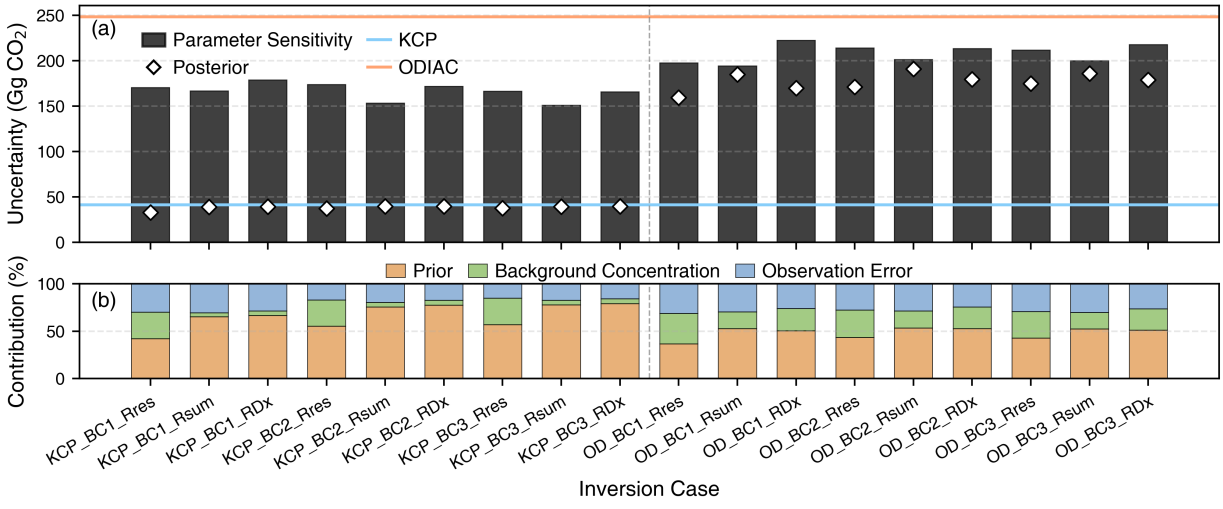


Figure 7. Comparison of daytime total parameter sensitivity and posterior uncertainty across the 18 configurations. (a) Parameter sensitivity (bars) and posterior uncertainty (diamonds) for each case. Prior uncertainties are shown as horizontal line for KCP (blue) and ODIAC (orange). (b) Relative contribution of each parameter assumption to parameter sensitivity. Contributions were calculated as $\frac{\sum \sigma_i}{\sum parameter\ sensitivity} \times 100$ (%), where σ_i is the standard deviation of posterior emissions under different assumptions for parameter i.

As shown in Fig. 7b, the contribution to this sensitivity was predominantly attributed to prior emissions, followed by observation errors and background concentrations in most configurations. However, in inversion cases using the Rres method for observation error assumption, the background assumption showed a higher contribution than observation errors, particularly in cases using KCP as the prior. This difference can be explained by the Rres method, in which observation errors

https://doi.org/10.5194/egusphere-2026-5709
Preprint. Discussion started: 3 November 2026
© Author(s) 2026. CC BY 4.0 License.

are estimated using **z**, a variable that accounts for background concentrations, thus amplifying the sensitivity to background concentration assumptions.

3.4 Robustness of Posterior Emissions and the Inverse Modeling Framework for Seoul

We selected the robust posterior emission estimate for Seoul as the posterior exhibiting the lowest posterior uncertainty, highest agreement between posterior-simulated $\Delta CO_{2,\,mod}$ and observed $\Delta CO_{2,\,obs}$, and minimal parameter sensitivity. Considering posterior uncertainty, the analysis narrowed to the emission estimates derived using KCP as the prior. Among these, the KCP_BC3_Rsum case provided the most robust estimate of anthropogenic CO_2 emissions for Seoul in December 2021. It showed the lowest RMSE and MAE values among the KCP-based estimates (Fig. S14 and Fig. S15), as well as the smallest parameter sensitivity, at 151.2 Gg CO_2.

A comparison of the prior and posterior emissions of KCP_BC3_Rsum is shown in Fig. 8. The daytime total CO_2 emissions from KCP_BC3_Rsum were 584.0 Gg CO_2, representing a reduction of 40.7 Gg CO_2 compared to the KCP prior. This posterior total was also lower than the ODIAC, showing a consistent outcome with the majority of the inversion results, where 11 of the 18 posterior estimates were lower than both prior inventories. The mean daytime CO_2 emissions for the prior KCP and posterior were 37.1 μmol CO_2 m^{-2} s^{-1} and 34.7 μmol CO_2 m^{-2} s^{-1}, respectively, representing a 6.5 % decrease in average emissions relative to the prior. The posterior emissions for this case represented an 8.7 % correction from the prior emissions (Table 3).

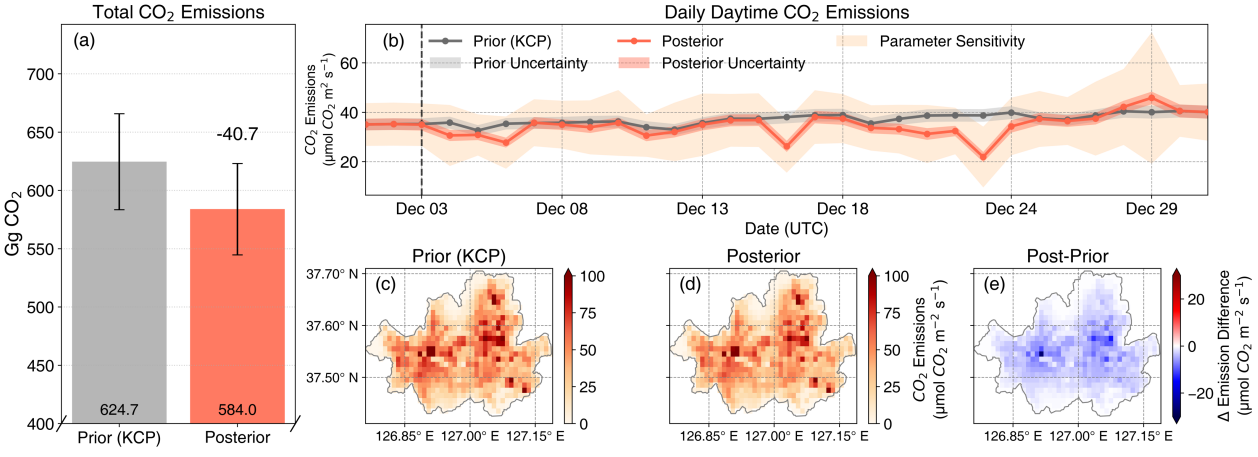


Figure 8. Relatively robust posterior emissions (KCP_BC3_Rsum) for daytime over Seoul in December 2021. (a) Total emissions and standard deviations for the prior (KCP) and posterior; (b–d) monthly mean spatial distribution of the (b) prior, (c) posterior, (d) emission correction (posterior-prior); (e) Time series of daytime–averaged CO_2 emissions with uncertainty and parameter sensitivity (shaded regions).

For the temporal variability of emissions, the temporal correlation between the prior KCP and the posterior emissions of KCP_BC3_Rsum was 0.42, indicating substantial changes in temporal patterns. As shown in Fig. 8b, a distinct decrease on December 23 and an increase on December 29 were consistently observed across all six cases using the Rsum method (Fig.

https://doi.org/10.5194/egusphere-2026-5709
Preprint. Discussion started: 3 November 2026
© Author(s) 2026. CC BY 4.0 License.

5). The prior KCP inventory, which applies a temporal scaling factor to account for activity patterns such as traffic emissions, exhibited clear weekday-weekend variations, with weekday mean daytime emissions of 37.6 (± 1.9) μmol CO_2 m^{-2} s^{-1} and weekend emissions of 35.6 (± 2.1) μmol CO_2 m^{-2} s^{-1}. After inversion, the most robust emissions showed weekday and weekend averages of 35.0 (± 5.0) μmol CO_2 m^{-2} s^{-1} and 33.6 (± 2.9) μmol CO_2 m^{-2} s^{-1}, respectively, indicating a slightly reduced difference between weekend and weekday emissions while variability within each period increased. E emission uncertainty decreased slightly from an average of 2.45 to 2.33 μmol CO_2 m^{-2} s^{-1}, while parameter sensitivity was larger, averaging 9.0 μmol CO_2 m^{-2} s^{-1}. Notably, parameter sensitivity was greatest during the increasing phase preceding the emission peak on December 29, particularly between December 27 and 29.

The inversion largely preserved the prior spatial emission pattern, with a spatial correlation of ≈ 1.00 between the monthly averaged optimal posterior emissions and KCP (Fig. 8c and Fig. 8d). As shown in Fig. 8e, the monthly averaged emissions correction decreased by approximately 10 μmol CO_2 m^{-2} s^{-1} throughout most of Seoul in proportion to the level of prior emissions with the exception of certain point sources in the northern and southeastern regions.

Finally, we evaluated the convergence of emission estimates for Seoul using the URR metric, which quantifies how much the spread among posterior estimates decreased or increased relative to the spread between two priors. A positive URR indicates effective convergence of the inversion system toward constrained flux estimates, whereas a negative URR implies increased divergence among posterior solutions, suggesting limited constraint by the inversion system. Fig. 9a shows the kernel density estimation of URR calculated from six posterior estimates for the two inversion cases generated by independently adjusting one assumption (prior emissions, background concentration, or observation error) within each case. OD_BC1_RDx, which had the largest parameter sensitivity, showed a median URR value of 0.06 and its kernel density estimation revealed that 51.8 % of its estimates converge (URR > 0) relative to the prior spread. KCP_BC3_Rsum, the relatively robust case with the smallest parameter sensitivity, showed substantially stronger convergence, with a median URR of 0.55 and 70.4 % of posterior fluxes indicating convergence. From the configuration with the smallest parameter sensitivity to that with the largest sensitivity, most of the estimates showed convergence. Although parameter sensitivity exceeded posterior uncertainty, the posterior estimates were generally constrained within a narrower range than the differences between the two priors across the various configurations. This reduction in spread indicates that the inversion for Seoul effectively constrained emissions against prior differences under the same observations.

https://doi.org/10.5194/egusphere-2026-5709
Preprint. Discussion started: 3 November 2026
© Author(s) 2026. CC BY 4.0 License.

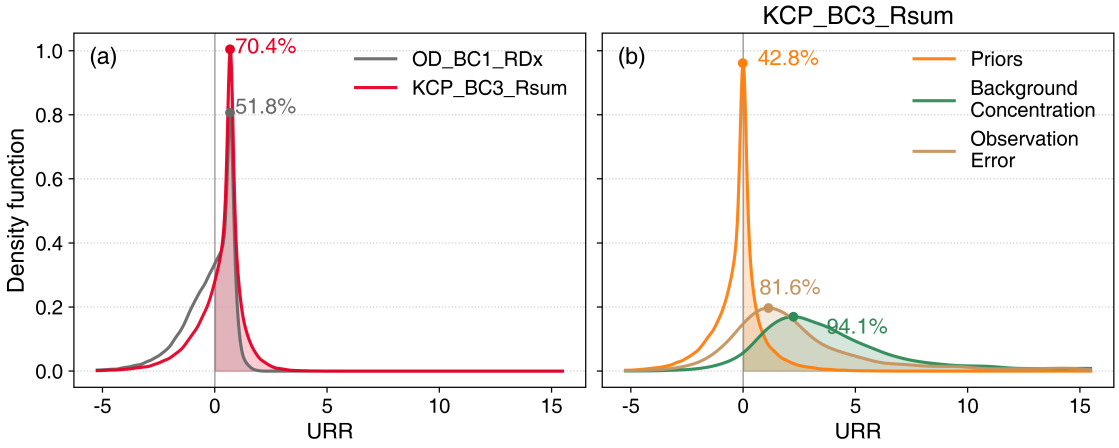


Figure 9. Kernel density estimation (KDE) of URR. (a) KDE of the highest parameter sensitivity case (OD_BC1_RDx) and the optimal estimate case (KCP_BC3_Rsum). (b) KDE of the URR (KCP_BC3_Rsum) obtained by varying each parameter individually.

Furthermore, to assess the impact of each input parameter assumption on the robustness of the inversion system, we analyzed the URR for KCP_BC3_Rsum when only the prior, background concentration, or observation error assumptions were individually adjusted (Fig. 9b). For background concentration and observation error, the median URR values were 3.21 and 1.71, respectively, with 94.1 % and 81.6 % of estimates showing strong convergence trends. These results revealed that the posterior estimates were robustly constrained by the differences between these two parameter assumptions. In contrast, for the choice of prior emissions, the median URR value was −0.03, and kernel density estimation showed that only 42.8 % of the estimates exhibited convergence. This indicates that KCP_BC3_Rsum retained a stronger dependence on the choice of prior inventory, consistent with the largest contribution of prior assumptions to parameter sensitivity, as shown in Fig. 7b. To identify why the choice of prior was less effectively constrained, we analyzed the time series of daily mean URR for KCP_BC3_Rsum under different prior assumptions (Fig. S16). Divergence between posterior estimates occurred when the degree of correction differed between the two cases using different priors. This suggests that differences in the prior error covariance values (**Q**) contributed to the differing correction strengths and consequently led to larger discrepancies in posterior emissions.

4 Discussion

Since this study revisited the December 2021 Seoul inversion case, a comparison with Sim and Jeong (2025) allowed us to examine both the agreements and discrepancies in posterior estimates. The results of this study were partially consistent with their findings. In particular, several inversion cases using ODIAC as the prior showed distinct reductions in eastern Seoul and increases in western Seoul, similar to the spatial correction patterns reported by Sim and Jeong (2025). The previous study attributed this pattern to ODIAC's nighttime-light based spatial disaggregation method, which likely led to an overestimation in residential-dominated eastern areas, with inverse modeling correcting this bias. Our intercomparison of inversion results

https://doi.org/10.5194/egusphere-2026-5709
Preprint. Discussion started: 3 November 2026
© Author(s) 2026. CC BY 4.0 License.

between ODIAC (nighttime light-based spatial allocation) and KCP (sector-based allocation) demonstrates that the correction pattern was more pronounced with ODIAC, thus supporting the results of Sim and Jeong (2025) that ODIAC's spatial allocation method exhibits this pronounced issue. However, the comprehensive intercomparison results indicate that the spatial correction patterns in Seoul are strongly influenced not only by the prior but also by the observation error and background concentration assumptions. For example, both the OD_BC1_Rsum and OD_BC2_Rsum cases exhibit a constraining east-west adjustment pattern (Fig. 6), while differences in background concentration result in variations in the spatial extent and intensity of corrections in the eastern and western regions. Furthermore, depending on the observation error assumptions, the case using Rres yields uniform reductions across Seoul, whereas the cases using RDx and Rsum show more east-west contrasting correction patterns. Thus, these results suggest that the east-west correction pattern reflects not only the ODIAC's spatial allocation method but also the influence of the background concentration and observation error assumptions.

For a robust posterior estimate, Sim and Jeong (2025) reported a 4.43 % increase relative to the ODIAC prior, while this study showed a 6.5 % decrease relative to the KCP prior. The resulting daytime mean emissions were 35.6 μmol CO_2 m^{-2} s^{-1} in Sim and Jeong (2025) and 34.7 μmol CO_2 m^{-2} s^{-1} in this study. The difference between the two posterior estimates was smaller than the initial difference between the KCP and ODIAC priors, suggesting that the inversion frameworks for Seoul constrained emission toward a similar range despite methodological differences. Differences remained in the monthly averaged spatial distribution and temporal variability of the posterior emissions, likely influenced by different prior emissions, background concentrations, observation error assumptions, and the use of different observational data (satellite data, the number of ground observations, and time window of assimilated observations). When comparing the most similar configuration, the OD_BC1_RDx case, which used the same prior emissions (ODIAC) as in the previous study, identical background concentration for ground observations, and the most similar diagnostic method for observation error assumptions, the result shows comparable spatiotemporal variability but not identical values, owing to differences in the assimilated time window of observations and the use of different observation datasets.

Rather than estimating urban CO_2 emissions, this study focused on methodological sensitivity. Therefore, the generalizability of the findings lies in the sensitivity patterns of the estimates identified among different parameter assumptions, rather than in the specific values obtained for Seoul. The results suggest that parameter assumptions selectively influence different components of posterior information, indicating that prior emissions, background concentrations, and observation errors play distinct roles within the inverse framework. This finding provides a basis for interpreting posterior estimates by identifying the influence of different parameter assumptions on posterior information. Furthermore, parameter sensitivity exceeded posterior uncertainty, indicating that posterior estimates derived from single inversion configuration may not fully represent the uncertainty associated with parameter assumptions. These results suggest that parameter sensitivity is a non-negligible in urban inverse modeling and emphasize the importance of methodological sensitivity analyses when interpreting posterior estimates. Consequently, metrics such as parameter sensitivity and URR can be used to identify robust posterior emissions and evaluate the robustness of the inversion framework for a given city.

https://doi.org/10.5194/egusphere-2026-5709
Preprint. Discussion started: 3 November 2026
© Author(s) 2026. CC BY 4.0 License.

5 Conclusions

Urban CO_2 inverse modeling studies often differ not only in parameter values but also in methodological assumptions regarding priors, background concentrations, and observation error covariance. This study shows that these assumptions control different components of posterior information including total emissions, temporal variability, and spatial distribution. Specifically, observation error assumptions had the largest influence on total emissions and temporal variability, whereas the spatial distribution of posterior emissions was predominantly determined by the choice of prior emissions. The assumption-dependent sensitivity of the posterior emissions for Seoul in December 2021 ranged from 26 % to 52 % of total emissions, exceeding the posterior uncertainty estimated from individual inversion configurations. Based on this sensitivity test, we demonstrate that robust posterior emission estimates can be derived and that the robustness of the inverse modeling framework can be assessed under different parameter assumptions.

Several limitations should be noted in this study. First, because of the large uncertainties in nighttime PBL dynamics in WRF-STILT, only daytime observations were assimilated and analyzed. Second, this study considered three major sources of uncertainty (prior emissions, background concentrations, and observation error assumptions). Other potential sources of uncertainty, such as differences among atmospheric transport models, methods for defining prior error covariance, data assimilation methodologies, and observation types, were not explicitly examined.

Future work should extend the analysis beyond daytime to include periods with stronger temporal emission variability, such as rush hours, to better constrain urban CO_2 emission dynamics. To assess the generalizability of the sensitivity patterns identified in this controlled case study of Seoul in December 2021, future work should extend the framework to longer periods and different cities. Thus, applying the inversion over longer periods, including seasonal timescales, would help determine whether the influence of these parameter assumptions remains consistent and improve our understanding of uncertainty in urban inverse modelling. At the broader community level, systematic intercomparison frameworks for urban inverse modelling, analogous to global and regional efforts such as TransCom, RECCAP, and OCO-2 MIP, are required to evaluate and reduce uncertainties across cities while accounting for various sources of uncertainty. In addition, integrating multiple observational platforms, including satellite observations (e.g., OCO-2 and OCO-3), ground based networks, mobile measurements, and isotope-based observations, together with independent validation datasets, would further improve the reliability of urban CO_2 emission estimates.

Data availability

The KCP prior emissions data and biogenic CO_2 fluxes data from the CASS were obtained from the Korea Carbon Project website (https://korea-carbon-project.org/map, last access: 15 January 2026). The ODIAC prior emissions data are available from the Center for Global Environmental Research (https://db.cger.nies.go.jp/dataset/ODIAC, last access: 20 January 2026). The ERA5 reanalysis product can be retrieved from the Copernicus Climate Change Service Climate Data Store (https://cds.climate.copernicus.eu/datasets/reanalysis-era5-single-levels?tab=download, last access: 22 February 2026). The

https://doi.org/10.5194/egusphere-2026-5709
Preprint. Discussion started: 3 November 2026
© Author(s) 2026. CC BY 4.0 License.

ASOS data were downloaded from Korea Meteorological Administration (https://data.kma.go.kr/resources/html/en/aowdp.html, last access: 12 November 2025) and OSTIA data were obtained from Copernicus Marine Data Store (https://data.marine.copernicus.eu/product/SST_GLO_SST_L4_NRT_OBSERVATIONS_010_001/services, last access: 10 November 2025).

Author contributions

SJ supervised the research and guided the analysis. SS developed the inverse modelling framework. SS and MP designed the experiments, and MP carried them out. MP analyzed the data and wrote the manuscript.

Competing interests

The authors declare that they have no conflict of interests.

Acknowledgements

This study was supported by Korea Environment Industry & Technology Institute (KEITI) through Project for developing an observation-based GHG emissions geospatial information map, funded by Korea Ministry of Climate, Energy and Environment (MCEE) (RS-2023-00232066), and by a grant from the National Institute of Environment Research (NIER), funded by Korea Ministry of Climate, Energy and Environment (MCEE) of the Republic of Korea (NIER-2026-05-02-006).

References

Arioli, M. S., D'Agosto, M. D. A., Amaral, F. G., and Cybis, H. B. B.: The evolution of city-scale GHG emissions inventory methods: a systematic review, Environmental Impact Assessment Review, 80, 106316, https://doi.org/10.1016/j.eiar.2019.106316 , 2020.

Bai, X., Dawson, R. J., Ürge-Vorsatz, D., Delgado, G. C., Salisu Barau, A., Dhakal, S., Dodman, D., Leonardsen, L., Masson-Delmotte, V., Roberts, D. C., Schultz, S., and Seto, K. C.: Six research priorities for cities and climate change, Nature, 555, 23–25, https://doi.org/10.1038/d41586-018-02409-z, 2018.

Bréon, F. M., Broquet, G., Puygrenier, V., Chevallier, F., Xueref-Remy, I., Ramonet, M., Dieudonné, E., Lopez, M., Schmidt, M., Perrussel, O., Ciais, P., and Meunier, F.: An attempt at estimating Paris area CO_2 emissions from atmospheric concentration measurements, Atmos. Chem. Phys., 15, 1707–1724, https://doi.org/10.5194/acp-15-1707-2015, 2015.

https://doi.org/10.5194/egusphere-2026-5709
Preprint. Discussion started: 3 November 2026
© Author(s) 2026. CC BY 4.0 License.

690 Cai, M., Shi, Y., and Ren, C.: Developing a high-resolution emission inventory tool for low-carbon city management using hybrid method–A pilot test in high-density Hong Kong, Energy Build., 226, 110376, https://doi.org/10.1016/j.enbuild.2020.110376, 2020.

Cai, Z., Hu, L., Chen, D., Ma, M., Hu, Q., Zhou, H., Chen, H., Yang, D., Li, Y., and Fang, X.: Atmosphere-based estimations of CO_2 emissions at city and county scales and comparative analysis: A case study in Yangtze River Delta Urban 695 Agglomerations (YRDUA), Environ. Res., 121930, https://doi.org/10.1016/j.envres.2025.121930, 2025.

Chandra, N., Patra, P. K., Niwa, Y., Ito, A., Iida, Y., Goto, D., Morimoto, S., Kondo, M., Takigawa, M., and Hajima, T.: Estimated regional CO2 flux and uncertainty based on an ensemble of atmospheric CO_2 inversions, Atmos. Chem. Phys., 22, 9215–9243, https://doi.org/10.5194/acp-22-9215-2022, 2022.

Che, K., Cai, Z., Liu, Y., Wu, L., Yang, D., Chen, Y., Li, M., Wang, H., Zhang, Y., and Wang, P.: Lagrangian inversion of 700 anthropogenic CO_2 emissions from Beijing using differential column measurements, Environ. Res. Lett., 17, 075001, https://doi.org/10.1088/1748-9326/ac7477, 2022.

Che, K., Lauvaux, T., Taquet, N., Stremme, W., Xu, Y., Alberti, C., Lopez, M., García-Reynoso, A., Ciais, P., and Liu, Y.: CO_2 emissions estimate from Mexico City using ground- and space-based remote sensing, J. Geophys. Res. Atmos., 129, e2024JD041297, https://doi.org/10.1029/2024JD041297, 2024.

705 Cohen, J.: Statistical power analysis for the behavioral sciences, Routledge Academic, New York, NY, USA, https://doi.org/10.4324/9780203771587, 1988.

Crowell, S., Baker, D., Schuh, A., Basu, S., Jacobson, A. R., Chevallier, F., Liu, J., Deng, F., Feng, L., and McKain, K.: The 2015–2016 carbon cycle as seen from OCO-2 and the global in situ network, Atmos. Chem. Phys., 19, 9797–9831, https://doi.org/10.5194/acp-19-9797-2019, 2019.

710 C40: C40 Annual Report 2024, C40 Cities Climate Leadership Group, https://www.c40.org/about-c40/#annualreport, (last access: 24 June 2026), 2025.

Desroziers, G., Berre, L., Chapnik, B., and Poli, P.: Diagnosis of observation, background and analysis-error statistics in observation space, Q. J. Roy. Meteor. Soc., 131, 3385–3396, https://doi.org/10.1256/qj.05.108, 2005.

Dilling, L., Doney, S. C., Edmonds, J., Gurney, K. R., Harriss, R., Schimel, D., and Stokes, G.: The role of carbon cycle 715 observations and knowledge in carbon management, Annu. Rev. Environ. Resour., 28, 521–558, https://doi.org/10.1146/annurev.energy.28.011503.163443, 2003.

Enting, I. G.: Inverse problems in atmospheric constituent transport, Cambridge University Press, Cambridge, United Kingdom, ISBN 978051153574, https://doi.org/10.1017/CBO9780511535741 , 2002.

European Commission: EU mission, climate-neutral and smart cities, Directorate-General for Research and Innovation, 720 Publications Office of the European Union, https://doi.org/10.2777/2538881 , 2025.

Fasoli, B., Lin, J. C., Bowling, D. R., Mitchell, L., and Mendoza, D.: Simulating atmospheric tracer concentrations for spatially distributed receptors: updates to the Stochastic Time-Inverted Lagrangian Transport model's R interface (STILT-R version 2), Geosci. Model Dev., 11, 2813–2824, https://doi.org/10.5194/gmd-11-2813-2018 , 2018.

https://doi.org/10.5194/egusphere-2026-5709
Preprint. Discussion started: 3 November 2026
© Author(s) 2026. CC BY 4.0 License.

Gately, C. K. and Hutyra, L. R.: Large uncertainties in urban-scale carbon emissions, J. Geophys. Res. Atmos., 122, 242–260, https://doi.org/10.1002/2017JD027359, 2017.

Gilfillan, D. and Marland, G.: CDIAC-FF: global and national CO_2 emissions from fossil fuel combustion and cement manufacture: 1751–2017, Earth Syst. Sci. Data, 13, 1667–1680, https://doi.org/10.5194/essd-13-1667-2021, 2021.

Gurney, K. R., Law, R. M., Denning, A. S., Rayner, P. J., Baker, D., Bousquet, P., Bruhwiler, L., Chen, Y.-H., Ciais, P., and Fan, S.: TransCom 3 CO2 inversion intercomparison: 1. Annual mean control results and sensitivity to transport and prior flux information, Tellus B, 55, 555–579, https://doi.org/10.3402/tellusb.v55i2.16728, 2003.

Gurney, K. R., Liang, J., O'Keeffe, D., Patarasuk, R., Hutchins, M., Huang, J., Song, Y., and Roest, G.: Comparison of global downscaled versus bottom-up fossil fuel CO2 emissions at the urban scale in four US urban areas, J. Geophys. Res. Atmos., 124, 2823–2840, https://doi.org/10.1029/2018JD028859, 2019.

Hamilton, S. D., Wu, D., Johnson, M. S., Turner, A. J., Fischer, M. L., Dadheech, N., and Jeong, S.: Estimating carbon dioxide emissions in two California cities using Bayesian inversion and satellite measurements, Geophys. Res. Lett., 51, e2024GL111150, https://doi.org/10.1029/2024GL111150, 2024.

He, C., Ji, M., Grieneisen, M. L., and Zhan, Y.: A review of datasets and methods for deriving spatiotemporal distributions of atmospheric CO_2, J. Environ. Manage., 322, 116101, https://doi.org/10.1016/j.jenvman.2022.116101, 2022.

Heald, C. L., Jacob, D. J., Jones, D. B., Palmer, P. I., Logan, J. A., Streets, D. G., Sachse, G. W., Gille, J. C., Hoffman, R. N., and Nehrkorn, T.: Comparative inverse analysis of satellite (MOPITT) and aircraft (TRACE-P) observations to estimate Asian sources of carbon monoxide, J. Geophys. Res. Atmos., 109, D23306, https://doi.org/10.1029/2004JD005185, 2004.

Hollingsworth, A. and Lönnberg, P.: The statistical structure of short-range forecast errors as determined from radiosonde data – Part I: The wind field, Tellus A, 38A, 111–136, https://doi.org/10.1111/j.1600-0870.1986.tb00460.x , 1986.

Hong, S. O., Kim, J., Byun, Y. H., Kim, Y. P., Park, S. B., and Kim, S.: Intra-urban variations of the CO_2 fluxes at the surface–atmosphere interface in the Seoul metropolitan area, Asia-Pac. J. Atmos. Sci., 59, 417–431, https://doi.org/10.1007/s13143-023-00324-6, 2023.

International Energy Agency (IEA): *Empowering Urban Energy Transitions*, IEA, Paris, https://www.iea.org/reports/empowering-urban-energy-transitions, 2024

IPCC: Climate Change 2022: Mitigation of Climate Change. Contribution of Working Group III to the Sixth Assessment Report of the Intergovernmental Panel on Climate Change, Cambridge University Press, Cambridge, United Kingdom and New York, NY, USA, https://doi.org/10.1017/9781009157926, 2022.

Jones, T. S., Franklin, J. E., Chen, J., Dietrich, F., Hajny, K. D., Paetzold, J. C., Kort, E. A., McKain, K., Ren, X., Sweeney, C., and Wofsy, S. C.: Assessing urban methane emissions using column-observing portable Fourier transform infrared (FTIR) spectrometers and a novel Bayesian inversion framework, Atmos. Chem. Phys., 21, 13131–13147, https://doi.org/10.5194/acp-21-13131-2021, 2021.

Kim, H., Kang, J. H., and Kwon, I. H.: Diagnostics of observation error of satellite radiance data in Korean Integrated Model (KIM) data assimilation system, Atmosphere, 32, 263–276, https://doi.org/10.14191/Atmos.2022.32.4.263, 2022.

https://doi.org/10.5194/egusphere-2026-5709
Preprint. Discussion started: 3 November 2026
© Author(s) 2026. CC BY 4.0 License.

Kong, Y., Zheng, B., Zhang, Q., and He, K.: Global and regional carbon budget for 2015–2020 inferred from OCO-2 based on an ensemble Kalman filter coupled with GEOS-Chem, Atmos. Chem. Phys., 22, 10769–10788, https://doi.org/10.5194/acp-22-10769-2022, 2022.

Korea Forest Service: Statistical Yearbook of Forestry 2021, No. 51, Korea Forest Service, Daejeon, Republic of Korea, 460 pp., https://book.nifos.go.kr/$/10110/contents/5817230 (last access: 29 September 2026), 2021.

Kunik, L., Mallia, D. V., Gurney, K. R., Mendoza, D. L., Oda, T., and Lin, J. C.: Bayesian inverse estimation of urban CO_2 emissions: Results from a synthetic data simulation over Salt Lake City, UT, Elem. Sci. Anth., 7, 36, https://doi.org/10.1525/elementa.375, 2019.

Lakens, D.: Calculating and reporting effect sizes to facilitate cumulative science: A practical primer for t-tests and ANOVAs, Front. Psychol., 4, 863, https://doi.org/10.3389/fpsyg.2013.00863, 2013.

Lauvaux, T., Miles, N. L., Deng, A., Richardson, S. J., Cambaliza, M. O., Davis, K. J., Gaudet, B., Gurney, K. R., Huang, J., O'Keefe, D., Song, Y., Karion, A., Oda, T., Patarasuk, R., Razlivanov, I., Sarmiento, D., Shepson, P., Sweeney, C., Turnbull, J., and Wu, K.: High-resolution atmospheric inversion of urban CO_2 emissions during the dormant season of the Indianapolis Flux Experiment (INFLUX), J. Geophys. Res.-Atmos., 121, 5213–5236, https://doi.org/10.1002/2015JD024473, 2016.

Lee, H. W., Cha, Y. M., Lee, S. H., and Kim, D. H.: Impact of high-resolution sea surface temperatures on the simulated wind resources in the southeastern coast of the Korean Peninsula, J. Environ. Sci. Int., 19, 171–184, https://doi.org/10.5322/JES.2010.19.2.171, 2010.

Lian, J., Bréon, F. M., Broquet, G., Lauvaux, T., Zheng, B., Ramonet, M., Xueref-Remy, I., Ciais, P.: Sensitivity to the sources of uncertainties in the modeling of atmospheric CO2 concentration within and in the vicinity of Paris, Atmos. Chem. Phys., 21, 10707–10726, https://doi.org/10.5194/acp-21-10707-2021, 2021.

Lian, J., Lauvaux, T., Utard, H., Bréon, F. M., Broquet, G., Ramonet, M., Xueref-Remy, I., Delmotte, M., and Ciais, P.: Assessing the effectiveness of an urban CO2 monitoring network over the Paris region through the COVID-19 lockdown natural experiment, Environ. Sci. Technol., 56, 2153–2162, https://doi.org/10.1021/acs.est.1c04973, 2022.

Lian, J., Lauvaux, T., Utard, H., Bréon, F. M., Broquet, G., Ramonet, M., Xueref-Remy, I., Delmotte, M., and Ciais, P.: Can we use atmospheric CO2 measurements to verify emission trends reported by cities? Lessons from a 6-year atmospheric inversion over Paris, Atmos. Chem. Phys., 23, 8823–8835, https://doi.org/10.5194/acp-23-8823-2023, 2023.

Lin, J. C., Gerbig, C., Wofsy, S. C., Andrews, A. E., Daube, B. C., Davis, K. J., and Grainger, C. A.: A near-field tool for simulating the upstream influence of atmospheric observations: the Stochastic Time-Inverted Lagrangian Transport (STILT) model, J. Geophys. Res.-Atmos., 108, 4493, https://doi.org/10.1029/2002JD003161, 2003.

Liu, Z., He, C., Zhou, Y., and Wu, J.: How much of the world's land has been urbanized, really? A hierarchical framework for avoiding confusion, Landsc. Ecol., 29, 763–771, https://doi.org/10.1007/s10980-014-0034-y, 2014.

Lopez-Coto, I., Ren, X., Salmon, O. E., Karion, A., Shepson, P. B., Dickerson, R. R., Heimburger, A. M. F., Harvey, R. M., Stirm, B. H., and Whetstone, J. R.: Wintertime CO_2, CH_4, and CO emissions estimation for the Washington, DC–Baltimore

https://doi.org/10.5194/egusphere-2026-5709
Preprint. Discussion started: 3 November 2026
© Author(s) 2026. CC BY 4.0 License.

metropolitan area using an inverse modeling technique, Environ. Sci. Technol., 54, 2606–2614, https://doi.org/10.1021/acs.est.9b06619, 2020.

Luqman, M., Rayner, P.J., and Gurney, K.R.: On the impact of urbanisation on CO_2 emissions. npj Urban Sustain 3, 6, https://doi.org/10.1038/s42949-023-00084-2, 2023.

795 Machida, T., Matsueda, H., Sawa, Y., Nakagawa, Y., Hirotani, K., Kondo, N., Goto, K., Nakazawa, T., Ishikawa, K., and Ogawa, T.: Worldwide measurements of atmospheric CO_2 and other trace gas species using commercial airlines, J. Atmos. Ocean. Technol., 25, 1744–1754, https://doi.org/10.1175/2008JTECHA1082.1, 2008.

Mallia, D. V., Lin, J. C., Urbanski, S., Ehleringer, J., and Nehrkorn, T.: Impacts of upwind wildfire emissions on CO, CO2, and PM2.5 concentrations in Salt Lake City, Utah, J. Geophys. Res. Atmos., 120, 147–166,
800 https://doi.org/10.1002/2014JD022472, 2015.

Mallia, D. V., Mitchell, L. E., Kunik, L., Fasoli, B., Bares, R., Gurney, K. R., and Lin, J. C.: Constraining urban CO_2 emissions using mobile observations from a light rail public transit platform, Environ. Sci. Technol., 54, 15613–15621, https://doi.org/10.1021/acs.est.0c04388, 2020.

Mallia, D. V., Mitchell, L. E., Gonzalez Vidal, A. E., Wu, D., Kunik, L., and Lin, J. C.: Can we detect urban-scale CO2
805 emission changes within medium-sized cities?, J. Geophys. Res. Atmos., 128, e2023JD038686, https://doi.org/10.1029/2023JD038686, 2023.

Maness, H. L., Thurlow, M. E., McDonald, B. C., and Harley, R. A.: Estimates of CO_2 traffic emissions from mobile concentration measurements, J. Geophys. Res. Atmos., 120, 2087–2102, https://doi.org/10.1002/2014JD022876, 2015.

Mun, J., Lee, H. W., Jeon, W., and Lee, S. H.: Impact of meteorological initial input data on WRF simulation – Comparison
810 of ERA-Interim and FNL data, J. Environ. Sci. Int., 26, 1307–1319, https://doi.org/10.5322/JESI.2017.26.12.1307, 2017.

Nalini, K., Lauvaux, T., Abdallah, C., Lian, J., Ciais, P., Utard, H., Broquet, G., Bréon, F. M., Chevallier, F., Xueref-Remy, I., Delmotte, M., and Ramonet, M.: High-resolution Lagrangian inverse modeling of CO2 emissions over the Paris region during the first 2020 lockdown period, J. Geophys. Res. Atmos., 127, e2021JD036032, https://doi.org/10.1029/2021JD036032, 2022.

815 Nassar, R., Napier-Linton, L., Gurney, K. R., Andres, R. J., Oda, T., Vogel, F. R., and Deng, F.: Improving the temporal and spatial distribution of CO_2 emissions from global fossil fuel emission data sets, J. Geophys. Res. Atmos., 118, 917–933, https://doi.org/10.1029/2012JD018196, 2013.

Nathan, B., Lauvaux, T., Turnbull, J., and Gurney, K.: Investigations into the use of multi-species measurements for source apportionment of the Indianapolis fossil fuel CO2 signal, Elem. Sci. Anth., 6, 21, https://doi.org/10.1525/elementa.131, 2018.

820 Newman, S., Xu, X., Gurney, K. R., Hsu, Y. K., Li, K. F., Jiang, X., Keeling, R. F., Feng, S., Oda, T., Patarasuk, R., Zimnoch, M., Weiss, R. F., and Yung, Y. L.: Toward consistency between trends in bottom-up CO_2 emissions and top-down atmospheric measurements in the Los Angeles megacity, Atmos. Chem. Phys., 16, 3843–3863, https://doi.org/10.5194/acp-16-3843-2016, 2016.

https://doi.org/10.5194/egusphere-2026-5709
Preprint. Discussion started: 3 November 2026
© Author(s) 2026. CC BY 4.0 License.

Oda, T. and Maksyutov, S.: A very high-resolution (1 km × 1 km) global fossil fuel CO_2 emission inventory derived using a point source database and satellite observations of nighttime lights, Atmos. Chem. Phys., 11, 543–556, https://doi.org/10.5194/acp-11-543-2011, 2011.

Oda, T., Maksyutov, S., and Andres, R. J.: The Open-source Data Inventory for Anthropogenic CO_2, version 2016 (ODIAC2016): A global monthly fossil fuel CO_2 gridded emissions data product for tracer transport simulations and surface flux inversions, Earth Syst. Sci. Data, 10, 87–107, https://doi.org/10.5194/essd-10-87-2018, 2018.

Ohyama, H., Frey, M. M., Morino, I., Shiomi, K., Nishihashi, M., Miyauchi, T., Yamada, H., Saito, M., Wakasa, M., and Blumenstock, T.: Anthropogenic CO2 emission estimates in the Tokyo metropolitan area from ground-based CO_2 column observations, Atmos. Chem. Phys., 23, 15097–15119, https://doi.org/10.5194/acp-23-15097-2023, 2023.

Park, C., Jeong, S., Park, M. S., Park, H., Yun, J., Lee, S. S., and Park, S. H.: Spatiotemporal variations in urban CO_2 flux with land-use types in Seoul, Carbon Balance Manage., 17, 3, https://doi.org/10.1186/s13021-022-00206-w, 2022.

Peylin, P., Law, R. M., Gurney, K. R., Chevallier, F., Jacobson, A. R., Maki, T., Niwa, Y., Patra, P. K., Peters, W., Rayner, P. J., Rödenbeck, C., van der Laan-Luijkx, I. T., and Zhang, X.: Global atmospheric carbon budget: results from an ensemble of atmospheric CO2 inversions, Biogeosciences, 10, 6699–6720, https://doi.org/10.5194/bg-10-6699-2013, 2013.

Pisso, I., Patra, P. K., Takigawa, M., Machida, T., Matsueda, H., and Sawa, Y.: Assessing Lagrangian inverse modelling of urban anthropogenic CO_2 fluxes using in situ aircraft and ground-based measurements in the Tokyo area, Carbon Balance Manag., 14, 6, https://doi.org/10.1186/s13021-019-0118-8, 2019.

Pitt, J. R., Lopez-Coto, I., Hajny, K. D., Tomlin, J., Kaeser, R., Jayarathne, T., Kort, E. A., Ren, X., Kondo, M., Sweeney, C., Karion, A., and Shepson, P. B.: New York City greenhouse gas emissions estimated with inverse modeling of aircraft measurements, Elem. Sci. Anth., 10, 00082, https://doi.org/10.1525/elementa.2021.00082, 2022.

Ritchie, H., Samborska, V., and Roser, M.: Urbanization, Our World in Data, https://ourworldindata.org/urbanization (last access: 3 April 2026), 2024.

Rodgers, C. D.: Inverse methods for atmospheric sounding: theory and practice, Series on Atmospheric, Oceanic and Planetary Physics, Vol. 2, World Scientific, Singapore, https://doi.org/10.1142/3171, 2000.

Roten, D., Lin, J. C., Das, S., and Kort, E. A.: Constraining sector-specific CO_2 fluxes using space-based XCO_2 observations over the Los Angeles basin, Geophys. Res. Lett., 50, e2023GL104376, https://doi.org/10.1029/2023GL104376, 2023.

Rutherford, I. D.: Data assimilation by statistical interpolation of forecast error fields, J. Atmos. Sci., 29, 809–815, https://doi.org/10.1175/1520-0469(1972)029<0809:DABSIO>2.0.CO;2, 1972.

Sargent, M., Barrera, Y., Nehrkorn, T., Hutyra, L. R., Gately, C. K., Jones, T., McKain, K., Sweeney, C., Hegarty, J., Hardiman, B., Wang, J. A., and Wofsy, S. C.: Anthropogenic and biogenic CO_2 fluxes in the Boston urban region, P. Natl. Acad. Sci. USA, 115, 7491–7496, https://doi.org/10.1073/pnas.1803715115 , 2018.

Seto, K. C., Dhakal, S., Bigio, A., Blanco, H., Delgado, G. C., Dewar, D., Huang, L., Inaba, A., Kansal, A., Lwasa, S., McMahon, J. E., Müller, D. B., Murakami, J., Nagendra, H., and Ramaswami, A.: Human settlements, infrastructure and spatial planning, in: Climate Change 2014: Mitigation of Climate Change. Contribution of Working Group III to the Fifth

https://doi.org/10.5194/egusphere-2026-5709
Preprint. Discussion started: 3 November 2026
© Author(s) 2026. CC BY 4.0 License.

Assessment Report of the Intergovernmental Panel on Climate Change, edited by: Edenhofer, O., Pichs-Madruga, R., Sokona, Y., Farahani, E., Kadner, S., Seyboth, K., Adler, A., Baum, I., Brunner, S., Eickemeier, P., Kriemann, B., Savolainen, J., Schlömer, S., von Stechow, C., Zwickel, T., and Minx, J. C., Cambridge University Press, Cambridge, UK and New York, NY, USA, 923–1000, https://doi.org/10.1017/CBO9781107415416.018, 2014

Shahbazi, H., Mostafazade Abolmaali, A., Alizadeh, H., Salavati, H., Zokaei, H., Zandavi, R., Torbatian, S., Yazgi, D., and Hosseini, V.: An emission inventory update for Tehran: The difference between air pollution and greenhouse gas source contributions, Atmos. Res., 275, 106240, https://doi.org/10.1016/j.atmosres.2022.106240, 2022.

Sheng, M., Lei, L., Zeng, Z. C., Rao, W., Song, H., and Wu, C.: Global land 1° mapping dataset of XCO_2 from satellite observations of GOSAT and OCO-2 from 2009 to 2020, Big Earth Data, 7, 170–190, https://doi.org/10.1080/20964471.2022.2033149, 2023.

Sim, S. and Jeong, S.: Constraining urban fossil fuel CO_2 emissions in Seoul using combined ground and satellite observations with Bayesian inverse modelling, Atmos. Chem. Phys., 25, 18509–18526, https://doi.org/10.5194/acp-25-18509-2025, 2025.

Sówka, I. and Bezyk, Y.: Greenhouse gas emission accounting at urban level: a case study of the city of Wroclaw (Poland), Atmos. Pollut. Res., 9, 289–298, https://doi.org/10.1016/j.apr.2017.10.005, 2018.

Stohl, A., Seibert, P., Arduini, J., Eckhardt, S., Fraser, P., Greally, B. R., Lunder, C., Maione, M., Mühle, J., O'Doherty, S., Prinn, R. G., Reimann, S., Saito, T., Schmidbauer, N., Simmonds, P. G., Vollmer, M. K., Weiss, R. F., and Yokouchi, Y.: An analytical inversion method for determining regional and global emissions of greenhouse gases: Sensitivity studies and application to halocarbons, Atmos. Chem. Phys., 9, 1597–1620, https://doi.org/10.5194/acp-9-1597-2009, 2009.

Sun, X., Mi, Z., Sudmant, A., Coffman, D. M., Yang, P., and Wood, R.: Using crowdsourced data to estimate the carbon footprints of global cities, Adv. Appl. Energy, 8, 100111, https://doi.org/10.1016/j.adapen.2022.100111, 2022.

Tarantola, A.: Inverse problem theory: Methods for data fitting and model parameter estimation, Elsevier Science, Amsterdam, ISBN 0-444-42765-1, https://epubs.siam.org/doi/book/10.1137/1.9780898717921, 1987.

United Nations: World Urbanization Prospects 2025: Summary of Results, UN DESA/POP/2025/TR/NO. 12, New York, USA, https://desapublications.un.org/publications/world-urbanization-prospects-2025-summary-results, 2025.

UNFCCC: Report of the Conference of the Parties on its twenty-first session, held in Paris from 30 November to 13 December 2015, Addendum, Part two: Action taken by the Conference of the Parties at its twenty-first session, FCCC/CP/2015/10/Add.1, United Nations Framework Convention on Climate Change, https://unfccc.int/documents/9097, (last access: 29 September 2026), 2016.

Vardag, S. N. and Maiwald, R.: Optimising urban measurement networks for CO_2 flux estimation: A high-resolution observing system simulation experiment using GRAMM/GRAL, Geosci. Model Dev., 17, 1885–1902, https://doi.org/10.5194/gmd-17-1885-2024, 2024.

Xie, J., Zhu, J., and Li, Y.: Assessment and inter-comparison of five high-resolution sea surface temperature products in the shelf and coastal seas around China, Cont. Shelf Res., 28, 1286–1293, https://doi.org/10.1016/j.csr.2008.02.020, 2008.

https://doi.org/10.5194/egusphere-2026-5709
Preprint. Discussion started: 3 November 2026
© Author(s) 2026. CC BY 4.0 License.



Yadav, V. and Michalak, A. M.: Improving computational efficiency in large linear inverse problems: An example from carbon dioxide flux estimation, Geosci. Model Dev., 6, 583–590, https://doi.org/10.5194/gmd-6-583-2013, 2013.

Zhang, L., Jiang, F., He, W., Wu, M., Wang, J., Ju, W., Wang, H., Zhang, Y., Sitch, S., and Chen, J. M.: Improved estimates of net ecosystem exchanges in mega-countries using GOSAT and OCO-2 observations, Commun. Earth Environ., 5, 737, https://doi.org/10.1038/s43247-024-01910-w, 2024.